The Development of a Novel Multi-modality Heart Phantom for Cardiac Applications in Radiotherapy

Kenneth W. Gregg

A thesis submitted in partial fulfillment of
the requirements for the degree of

Master of Science
(Medical Physics)

at the

UNIVERSITY OF WISCONSIN–MADISON

2023

Dedicated to all who have struggled with cancer,
including those I've come to know and lost.

With perseverance, we can learn, improve, and overcome.

Table of Contents

Acknowledgements

In the past two years at the University of Wisconsin–Madison, I have been fortunate to have the continued support of many faculty, staff, students, friends, and family. I humbly express my utmost gratitude to all those who have helped make this thesis successful. I have done my best to include all those who have selflessly contributed to this chapter of my life, be it scientifically or in support of me personally. The list is long and could be longer yet.

First, to my loving wife, Katie. My two years in Wisconsin would not have been nearly as successful if it were not for your help. The trips back and forth over long distance, to our wedding last summer, and now to our bright future together. I'm grateful to have your love and support every step of the way. You give me a reason to push forward and do things I never would have thought myself capable of otherwise. The journey I am taking is yours too, and I'm thankful to have you by my side through it all.

Next, to the best advisor I could have asked for, Dr. Carri Glide-Hurst. You've continually encouraged me to think scientifically and creatively, always helping me strive for better and better. I'm truly thankful for you spurring me on to create a phantom with the most utility and flexibility for future uses in the clinic. I'm so excited to be in the process of applying for a patent on this new technology and hope it will be used to do great things. Aside from helping with the technical details of this project, you have guided and encouraged me in professional development which will be helpful in any environment. Through the past year of developing connections, submitting abstracts, and residency applications. I'm glad to have had you as my PI. My future is bright due to all the work you've put in to guide me this past year.

The members of the Glide-Hurst lab are some of the most intelligent and honest, hard-working people I've come to know in my studies. Nicholas was key in connecting me with Carri

after helping me look for my lost cat. He has helped answer questions whenever I needed help with code or computers. Yuhao has been there to answer some of the silly technical questions about MRI I felt too embarrassed to ask Carri. Chase is currently working with Tarun in the Wieben lab on evaluating cardiac motion with 5D MRI data to help with motion considerations for my design. All of you have been a treasure to work with and I'm sure you will all do excellent in your future.

Industry partner Modus Medical has been very helpful in the fabrication of the phantom housing. While the phantom is not fabricated yet, I'm hoping it will be very useful and allow us to perform novel experiments over the summer for my first publication. I appreciate everyone at the company who has been attentive at our meetings and the positive, expert feedback from them for the past year. This work would not have been possible without the NIH R01HL 153720 grant which has funded this project and collaboration with Modus.

For the past year, I've had the opportunity to work with some Biomedical Engineering (BME) design students. Margo, Gracie, and Cam have been instrumental in most of the 3D printing activities for this thesis and performed the mechanical testing for the deformable evaluations in Chapter 6. They've been a valuable resource and are continuing to help create the first modular heart model.

A few more people I am thankful for in this work include Dr. Wesley Culberson and Dr. Jordan Slagowski who have agreed to participate in the defense and review of this thesis. Thanks also to Dr. Prashant Nagpal, the cardiovascular radiologist who helped review the cardiac contours. And another thank-you to Jami Wood for being the chaos coordinator, helping schedule (some last-minute) meetings, booking rooms, and ordering food for lab meetings.

My parents, mentors, teachers, and undergraduate education all developed a strong

foundation for the successful research I’ve completed at the University of Wisconsin. I’m thankful to have grown up in a home with a dad as an engineer who would explain every little thing I asked about. Two of my mentors and close friends Jim Duck and Char Messenger, thank you for sticking by me and believing in me. My high school physics teacher, Paul Dillick, encouraged me to pursue both engineering and physics while an undergrad to just keep my options open. I would not have the unique skillset now without your guidance and the intelligent professors who taught me during my time at the University of Akron.

The University of Wisconsin graduate program in medical physics has been rigorous but has been worth every moment. The long assignments and complex lectures have enriched my understanding of the field and will be a resource I look back on to help me in my career as a medical physicist. This is a quick mention to all the professors past and present who have worked to make the program as prestigious as it is.

There are surely many more names of people behind the scenes who could be listed in these Acknowledgements. If you are one of them, know that I am forever grateful for your help in my life. I will continue to work my hardest with the utmost perseverance to run the race that is set before me, knowing the many people who have helped me along the way are proud of where this has led, and where we still have yet to go.

On Wisconsin!

Abstract

Purpose & Introduction:

For radiotherapy in the thoracic region and radioablation of non-cancerous conditions such as ventricular tachycardia (VT), geometric and dosimetric accuracy near the beating heart is critical. For this project, a flexible multi-modality heart phantom was designed which incorporates cardio-respiratory motion and novel scintillation detectors to facilitate high-precision radiotherapy in the thoracic region. Eight essential design goals were developed according to physicist user needs for the project: (1) the CT number of the heart material should be close to myocardium; (2) the system must be MR-compatible; (3) the phantom must be durable, withstanding many usage cycles; (4) the design must be water-compatible; (5) the heart model must move according to both cardiac and respiratory influences; (6) the heart model must be anthropomorphic and include at least 12 heart substructures; (7) the prototype design should be compatible with current clinical equipment; (8) the prototype design should allow for dosimetry at several locations throughout the model.

Material specifications were developed from the design goals and weighted using a 1-5 scale of importance, to inform a decision matrix for evaluating five candidate materials. The weights were multiplied by individual scores (1-5) evaluated from a literature review and divided by a maximum score to obtain an overall score out of 5. Each material that is capable of being 3D-printed (3D-P) scored highly in the preliminary evaluation, where ease of fabrication and material durability drove the scoring rubric. The high scorers from this decision matrix guided the investigation toward further characterization of 3D-P materials.

Materials & Methods:

Five sample materials (Agilus30, Durometer 60, EPU 40, FPU50, SIL30) were printed

(5mmx50mm) and obtained from Midwest Prototyping. A second cardiac model was prototyped using Elastic50A on a FormLabs Form 3BL printer. Imaging experiments were performed using a CT-simulator, T1-weighted (T1W) and T2-weighted (T2W) sequences on a 1.5T MR-simulator, and T2W and true fast and steady precession (TrueFISP) sequences on a 0.35T MR-Linac. Three Elastic50A sample cylinders (2cm height, 2.5cm diameter) were obtained to perform non-destructive compression testing on a Material Testing System (MTS). Eight compression cycles were performed at a strain rate of 0.2 mm/s.

Twelve heart substructures were contoured following a published cardiac atlas on a contrast-enhanced CT with coronary angiography (CTCA) scan. The contours were verified by a cardiovascular radiologist and exported as an STL file using MIM Maestro. The heart model was simplified using the shrink-wrap feature in ANSYS Workbench to generate a mesh with 0.5cm element sizing. The boundary conditions for the test were chosen according to the maximum safe driving force of the MR-safe motor to match the expected design dynamics. The superior-most faces were held fixed while a force with magnitude 20N was applied upwards for a duration of 0.5s at the inferior-most faces.

A novel anthropomorphic phantom module has been simulated using 3D engineering design software. Multi-point scintillator dosimeter devices considered for the final fabrication of this module were validated in a low-field MR-linac using a similar motion phantom. Several gating parameters were tested to evaluate the efficacy of the novel dosimeters in future motion experiments.

Results:

The average CT numbers were Agilus30 (15 ± 22 HU), Durometer 60 (-37 ± 28 HU), EPU 40 (-57 ± 39 HU), FPU50 (51 ± 34 HU), SIL30 (20 ± 30 HU), and Elastic50A (38 ± 22 HU), with

Elastic50A most comparable to the average CT number of the human heart (39 ± 23 HU). All materials displayed a difference of signal to water in standard MRI sequences, allowing for image contrast against the water background. An Elastic50A 3D model was printed and imaged on all modalities, with the model's substructures appearing in each imaging modality. The experimentally-determined average compressive Young's modulus of Elastic50A is 3.87 ± 0.14 MPa. Using the compressive modulus, the Elastic50A heart phantom will be capable of deformable movement up to 0.44 ± 0.04 cm (k=2) at the apex, which is approximately equal to the centroid movement of the LV reported in the literature. The maximum simulated equivalent stress and strain were found to be 289 ± 26 kPa (k=2) and 8.3 ± 0.7% (k=2) respectively, at the outer wall of the superior pulmonary trunk. These values are less than the ultimate tensile strength and elongation at failure. Therefore, the material is not projected to fail under a compressive deformable load.

The simulated design has been retrofitted to a commercially available MR-safe ceramic motor for rigid motion. The programmable motor software allows for linear and rotational motion in decoupled respiratory and cardiac waveforms. A modified hollow body oval and cylindrical heart module has been designed to contain the heart for rigid movement. The design for the heart module has several openings to allow for the insertion of cavities that may contain a variety of objects for medical device inserts or dosimeters for determining radiation dose. Multi-point scintillation detectors have shown promise for reporting gating efficiency via the unique real-time readout of these dosimeters. No apparent image artifacts were observed when using the novel detectors, indicating acceptable use for future motion-gating experiments.

Conclusions & Future Work:

The initial prototyping has been performed for a novel 3D-printed heart model for use in

radiation therapy applications. Elastic50A was determined to be the optimal material of choice due to its similarities to heart tissue in CT and contrast to water in MRI. A novel multi-modality anthropomorphic heart phantom has been designed for integration with validated scintillation dosimeters for cardiac applications in radiotherapy. Future work includes the fabrication of the phantom module and experimental testing. The flexible nature of the material allows for deformable motion to be considered for future design iterations.

List of Tables

List of Figures

1 | Introduction

1.1 Clinical Motivation

According to recent statistics given by the American Cancer Society, cancer remained the second-leading cause of death in the United States even considering the impact of the COVID-19 pandemic, accounting for 18% of deaths in 2022. [1] Breast and lung cancers continue to be the most common cancer-related cause of death in the United States; in 2023, an estimated half-million people will be diagnosed with lung and bronchus or female breast cancer, and an estimated ~170,000 deaths will occur from these cancers. [1] While the field strives to reduce mortality due to cancer, considerations must also be made to reduce potential negative effects (e.g., treatment-related toxicities) to improve long term patient outcomes. This motivates study in the avoidance of vital organs such as the heart, as radiation therapy (RT) delivered near the heart has been linked to both acute and late effects including radiation-induced cardiovascular disease. [2]

Radiation-induced coronary artery disease (RICAD) is among the most common causes of morbidity and mortality of patients receiving radiation therapy in the thoracic region. [3] Epidemiology studies suggest late effects of radiation exposure from RT to conditions such as breast cancer (BC), Hodgkin's lymphoma (HL), [4] lung cancer, esophageal cancer, and thymoma [5] are likely to be associated with RICAD. HL survivors who have received radiation treatment have 2.5 times increased risk of developing CAD later in life. [6] BC patients receiving radiation treatment average 0.25 times increased risk. [3] Since BC patients often receive lower doses of radiation, RICAD has been further investigated and proposed to be a dose-dependent late effect of radiotherapy in the thoracic region. [7]

Mediastinal RT is known to cause radiotoxicity to other anatomies and internal substructures of the heart as well, incurring damage to the valves, myocardium, and pericardium causing aortic regurgitation, pericardial disease, pericardial effusion, and cardiomyopathy. [2] In some rare cases, radiation may cause acute pericarditis known to present as early as several days after treatment of HL. [8]

Each of the negative effects discussed here is caused by ionizing radiation in the thoracic region in life-saving cancer treatments. The therapeutic ratio is defined as "the relationship between the probability of tumor control and the likelihood of tissue damage," [9] and is a major consideration for clinical radiotherapy procedures—especially those which are near a critical Organ-At-Risk (OAR) such as the heart. Cardiac sparing in radiation therapy is an active area of research which aims to maximize the therapeutic ratio in thoracic cancer treatments by reducing radiation dose to the radiosensitive heart and its internal substructures. Clinical standards proposed by the Quantitative Analyses of Normal Tissue Effects in the Clinic (QUANTEC) advised in 2010 that less than 10% of the whole heart volume should receive 25 Gy radiation to reduce the chance for cardiac mortality within ~15 years to less than 1%. [10] While these guidelines are still in use today, more recent studies suggest some heart substructures are more radiosensitive than others and recognize the QUANTEC guidelines may have underestimated the late-effects of radiation to the heart—perhaps due to lack of studies involving lung cancer treatments, lack of heart substructure contouring, confounding risk factors, and insufficient data for evaluating dose-volume dependencies. [11]

One example is in a 5-year follow-up for overall survival (OS) analysis of the NRG Oncology RTOG 0617 trial investigating the effects of high dose (74 Gy) and standard dose (60 Gy) chemoradiotherapy for non-small lung cancer. [12] The study agreed with consensus for whole heart metrics; greater radiation dose to 5% of the heart volume (v5) results in lower OS. [12] However, deeper statistical analysis performed on this trial revealed that cardiac substructure exposure to radiation is a better predictor of OS than the v5 or v30 dosage used in clinical treatment planning. [13] A number of recent studies for thoracic cancer treatments report that increased dose to cardiac substructures is correlated with regional cardiotoxicities, supporting the need for substructure-specific dose evaluations in radiotherapy planning for improved cardiac outcomes. [14]

Given the potential role of cardiac substructure dose in patient survival, methods are being developed for more effective cardiac sparing which involve incorporation of internal cardiac anatomy to radiation treatment planning rather than whole-heart dose metrics. This method is currently limited by the time-consuming task to manually delineate cardiac substructures. Recent technologies proposed to resolve this limitation include a knowledge-based planning (KBP) technique that uses plans generated with cardiac substructures to train treatment planning optimization to rapidly output treatment plans with more effective cardiac sparing. [15] Another approach uses artificial intelligence with deep-learning methods to delineate heart substructures to replace manual contouring of the substructures for cardiac sparing treatment plans. [16] These methods for improved cardiac substructure segmentation and subsequent sparing highlight an emerging clinical need for a cardiac phantom to validate these novel technologies.

While many resources are dedicated toward cardiac sparing, a technique is emerging in which radioablative doses on the order of 20 Gy are delivered to arrhythmogenic scar regions of the heart for noninvasive treatment of high-risk refractory ventricular tachycardia (VT). [17] A recent multi-institutional clinical trial has been opened to study a larger cohort of patients using cardiac radioablation treatment. [18] The radiation for these treatments at UW Health is being delivered using a Varian TrueBeam Edge linear accelerator (linac) that has higher resolution multi-leaf collimators to provide superior precision to other linacs for more precisely treating cardiac scar tissue while maximally sparing the rest of the heart.

To maximize the therapeutic ratio, high geometric and dosimetric accuracy near the radiosensitive heart and its substructures is critical for cardiac sparing in the thoracic region and cardiac radioablation for the treatment of ventricular tachycardia. The goal of this thesis is to contribute meaningfully to these emerging cardiac applications of radiotherapy. The projected outcome is a completed prototype design for a novel anthropomorphic heart phantom that can be imaged in multiple modalities including MRI and CT. This phantom will also incorporate motion using a clinically available MR-safe programmable motor capable of movement in the superior-inferior direction, as well as twisting for out-of-plane excursions. Interchangeable inserts will make the design dosimetry-capable and flexible to target multiple points of measurement for dose evaluations of RT treatments. To present knowledge, this phantom will be the first to incorporate key features that are essential for facilitating high precision radiation therapy in cardiac applications.

1.2 Overview of Upcoming Chapters

Relevant background to the project is introduced in Chapter 2 which includes a description of an MR-safe motor available in the UW clinic, a characterization of cardiac and respiratory motion from literature, recent advancements in gated radiotherapy, and a review of prior art similar to the phantom developed in this work. The review highlights some limitations of the current phantoms which are addressed by the novel design. The design process then began with preliminary evaluations including a user needs profile and the determination of eight essential design goals described in Chapter 3. The design goals were translated into several material specifications used for a material decision matrix informed by a literature review. The completed decision matrix indicated that 3D-printing materials are best suited to fulfill the design goals.

In Chapter 4, several 3D-printed samples were obtained and imaged on a Computed

Tomography Simulator (CT-SIM), a 1.5T Magnetic Resonance Imaging Simulator (MR-SIM), and a 0.35T Magnetic Resonance Imaging Linear Accelerator (MR-linac). Average CT Numbers (Hounsfield Units, HU) for the 3D-printing materials were reported and compared to reference cardiac tissues, while the materials were evaluated against water background in MRI. Chapter 5 describes the development of a patient-specific 3D cardiac model derived from a contrast-enhanced Computed Tomography Coronary Angiogram (CTCA). Post-processing and initial fabrication results are described. Mechanical testing of the final candidate model was carried out in Chapter 6 to evaluate the feasibility of this material to be incorporated in deforming anatomical geometries. Material compression testing and material data sheets gave engineering information to complete a deformable Finite Element Analysis (FEA) with applied boundary conditions that reflect expected design dynamics. Total deformation was compared to LV centroid displacement in literature. Stresses and strains were compared to the ultimate stress and strain at break to evaluate the ability of the material to withstand the deformation.

A modular phantom was then designed with capabilities for rigid motion and dosimetry that interfaces with the current clinical equipment. Engineering renderings of the novel invention are introduced and discussed in Chapter 7 and an end-to-end experiment was designed. The last section of this chapter describes a completed experiment for the first use of novel real-time multi-point scintillation detectors in gating experiments in a low-field MR-linac. Chapter 8 describes a discussion of the limitations of the finished evaluations and future work. The culmination of the work ends with a comprehensive experimental design to be completed with the phantom module to be conducted.

Some of the works described in this thesis have been accepted for academic presentations or are being considered for a patent application. Works from Chapters 2-5 were developed into an abstract accepted for an oral presentation titled “Checking The Beat: Development of a Novel Multi-Modality Heart Phantom for Cardiac Applications in Radiation Therapy” at the AAPM Annual Meeting scheduled for July 2023. An abstract describing the key methods and results from the scintillator experiment in Chapter 7 was accepted for a SNAP oral titled “First Gating Validation Results in a Low-field MR-Linac Using Novel Multi-Point Plastic Scintillation Detectors” also to be given at the AAPM Annual Meeting in July 2023. An invention disclosure for the novel modular phantom design was submitted to Wisconsin Alumni Research Foundation (WARF) and the technology has been accepted for preparation of a patent application as the “Flexible Modular Phantom and Method for Medical Applications Using Interchangeable Inserts” as of April 2023. The experiments outlined in Chapter 7 will be used for publication of a research article in an appropriate journal once the fabrication of the phantom has been completed.

2 | Background

2.1 Magnetic Resonance Imaging-Compatible Phantom and Motor

Magnetic Resonance Imaging (MRI) is an imaging modality that provides superior soft tissue contrast for a wide variety of applications and does not expose patients to ionizing radiation. While this non-ionizing imaging modality spares patients from exposure to high-energy electromagnetic radiation, there are still many precautions taken for the safe use of an MRI. Diagnostic scanners typically produce a high magnetic field strength of 1.5 or 3.0 Tesla, necessary for achieving net angular spin momentum of atomic nuclei allowing for radiofrequency (RF) pulses to noninvasively probe patient anatomy to produce an image. While this imaging modality is powerful in the delineation of soft tissues, the high magnetic field presents a considerable challenge when working in such an environment. Any item that contains ferrous material will present safety risks, and most modern electronics will confound the imaging with artifacts or quit working in the presence of this strong magnetic field. Therefore, in the creation of a multi-modality phantom, the use of MRI presents the most design constraints due to the strong magnetic field necessary for creating images.

In the construction of this moving phantom, the QUASAR™ MRI^{4D} Motion Phantom produced by Modus Medical Devices Inc. (London, ON) will be utilized. This apparatus includes a programmable MR-safe motor capable of two degrees of freedom (linear and rotational) controlled by proprietary software. This software allows user control of the position as a function of time, with a recent capability of applying multiple decoupled motion profiles at once. The motor attaches to a dovetail plate interface on the front of a water-filled hollow body oval (Figure 1). When the apparatus is set up on a standard linear accelerator (linac) couch, the linear motion acts in the superoinferior (SI) direction and the rotational motion provides out-of-plane movement.

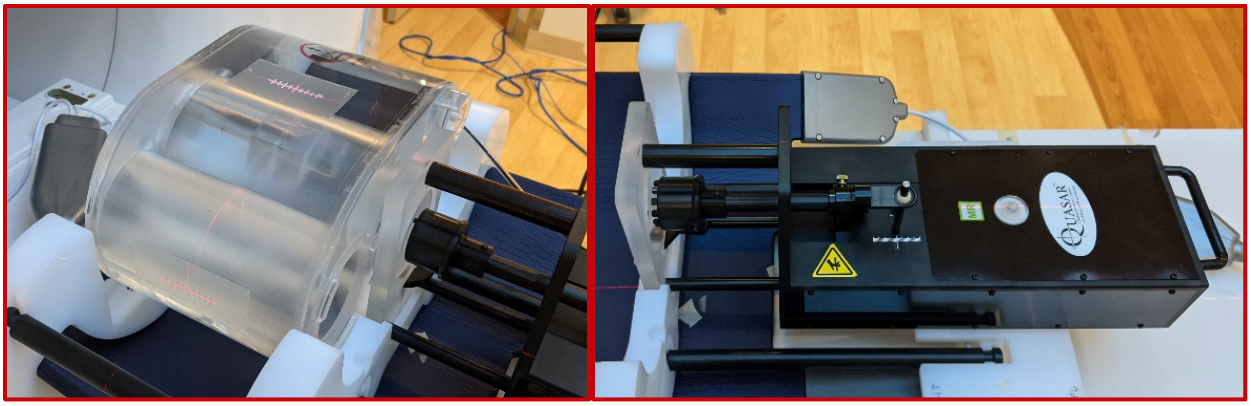

Figure 1. Photographs of the hollow body oval in a cradle with the MR-safe motor attached to the front face (left) and the whole MR-safe programmable motor shown separately (right).

Inside the hollow body oval is a cylindrical space where commercially available phantom inserts may be placed and attached to the MR-safe motor for research involving motion-gating in the UW clinic. The commercially-available inserts are currently limited to simple geometries including rods, spheres, cuboids, and ion chamber holders. [19] Given the importance of cardiac sparing and emerging treatments in radioablation of the heart, the goal of this work is to design and build a flexible, multi-modality heart phantom module with dosimetric capabilities that leverages the current clinical equipment and includes both cardiac and respiratory excursions to facilitate cardiac applications in high-precision radiotherapy.

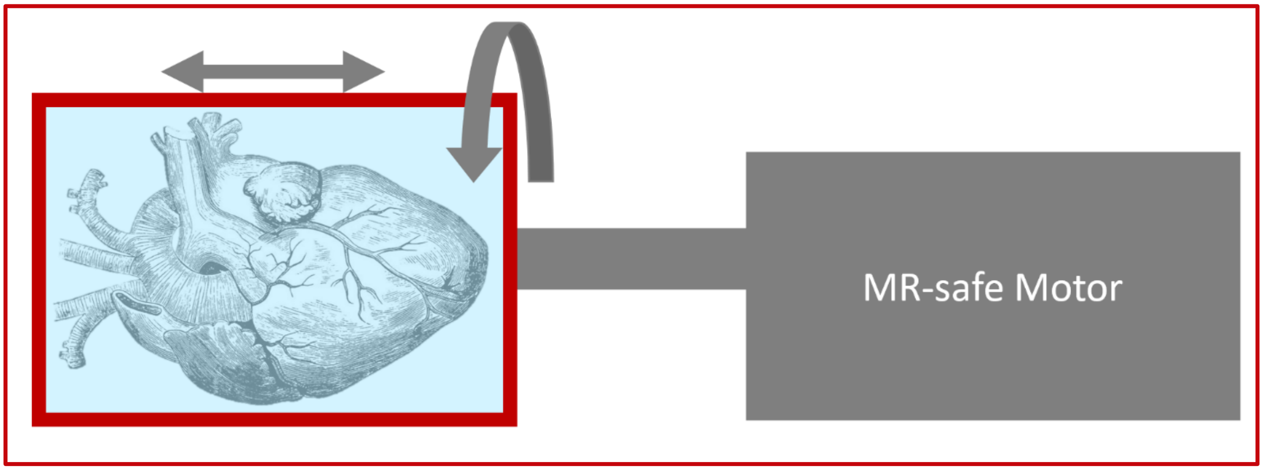

Figure 2. A simple diagram showing the proposed anthropomorphic heart phantom module to be inserted into the hollow body oval and connected to an MR-safe motor which provides both translational (SI) and rotational (out-of-plane) motion.

2.2 Characterization of Cardiac and Respiratory Motion

The current workflow for developing a 3D radiation treatment plan typically starts with a patient receiving a Computed Tomography (CT) scan on a CT simulator (CT-SIM). [20] CT-SIM systems are used to acquire images of the internal patient's anatomy while in the same position as what they would be during treatment. These images are used in conjunction with a radiation treatment planning system (TPS) to develop a personalized radiation delivery plan. [20] In the development of the treatment plan, healthy organs at risk (OARs) are identified by their proximity and sensitivity to the planning target volume (PTV) which is the target of radiation delivery. [21]

However, structures within the human body move between delivered fractions (interfraction motion) and during a single delivery (intrafraction motion). Interfraction motion is often due to differences in day-to-day patient positioning or slow-changing internal anatomies such as tumor shrinkage, or urinary and gastrointestinal filling and emptying. A common source of intrafraction motion in the thoracic region are muscle contractions of the diaphragm and myocardium which are necessary for breathing and distribution of blood to carry nutrients throughout the body, respectively. The majority of RT treatments account for these movements by assigning a margin around the OARs called a planning organ at risk volume (PRV) to mitigate the radiation exposure to this structure in the course of the radiation treatment. Another common technique to mitigate known as deep-inspiration breath hold (DIBH) may require patients to hold their breath for the duration of treatment to minimize these motions. The position of the critically radiosensitive heart is perpetually moving at high-frequencies (~70 beats per minute at rest) [22] due to the myocardium, and also influenced by lower frequencies (~15 breaths per minute at rest) [23, 24] due to the diaphragm. It is important to study the movement of this OAR to develop motion management techniques, create appropriate margins, and recreate these motions for designing a moving anthropomorphic phantom. [25]

The movement of the heart is attributed to the motion of the diaphragm and myocardium. The diaphragm is the muscle responsible for inspiration and exhalation, while the myocardium ejects blood in the cardiovascular cycle. Several works are reviewed below which provided insight into whole heart and heart substructure movements during free breathing (FB) and deep-inspiration breath-hold (DIBH) to develop a motion profile for decoupled heart and diaphragm movement to prescribe motion to the MR-safe programmable motor.

The study by Henke *et al* performed cine MRI to determine an average motion profile during FB and DIBH to construct whole-heart PRV margins to account for 98% of the motion (PRV-98) and 67% of the motion (PRV-67) in three anatomical planes, anteroposterior (AP), left-right (LR), and superoinferior (SI). The simplified PRV margins range from 3mm in the AP plane during DIBH for PRV-67, to 13mm in the SI plane during FB. [26] Ouyang *et al* reported on the motion of 6 cardiac substructures from patients who received cardiac-gated CT in preparation for transcatheter aortic valve replacement under voluntary breath-hold. Motion profiles from these data were reconstructed using the centroid position away from the time-averaged position in the 3 planes (AP, LR, SI). The findings report that cardiac motion is mostly within 5mm for each direction and recommends a 5mm expansion to OAR contours to produce a PRV contour. The data for the superoinferior centroid movement from the average position of the left ventricle (LV) during DIBH were extracted and then approximated using a spline fit (Figure 3, next page). [27]

Statistical analysis of diaphragm motion from fluoroscopic studies in Lujan *et al* supported parameterization of the SI position of the diaphragm (z) as a function of time (t) in the following equation [23]

$$z(t) = z_0 - b\cos^{2n}\left(\frac{\pi t}{\tau} - \phi\right) \tag{1}$$

where z_0 is the position at exhale, b is the amplitude of the motion, τ is the period of the breathing cycle, and n is an integer parameter that describes the asymmetry (flatness and steepness) of the breathing. The original model assumed a fixed period $\tau = 4.2s$, amplitude $b = 1.5cm$, and asymmetry $n = 3$. [23] A later consideration was made for variability in breathing depth and asymmetry, reporting that assumptions of $n = 2, 3, 6$ all seem to fit experimental data well. [24] A larger cohort study that supports this model has shown that $n = 2$ yields the best approximation for the average SI motion of the diaphragm, with period $\tau = 3.8s$ and amplitude $b = 1.64cm$. [28]

To prescribe SI motion mimicking both respiratory and cardiac-induced motion for an anthropomorphic phantom module, the above findings from the literature review were used. The SI motion of the LV centroid [27] approximated as a quadratic spline-fit at DIBH is overlayed with the parameterized position of the diaphragm given in Equation (1) using the average motion parameters (Figure 3). [28] While the mimicking of myocardial contraction is rate-limited by the capabilities of the MR-safe motor to 1 Hz (60 bpm), this is within the 95% C.I. (45-95 bpm, n=500) for normal resting heart rate reported by Spodick *et al.* [22] The approximate peak-to-peak motion using this cardiac waveform is 2mm, which may be an underestimation of overall heart movement based on recommended PRV margins. The flexibility of the motion configurations with the phantom allows for customization of the SI motion profile using patient-informed considerations. Since the waveforms are decoupled, the respiratory motion profile may be held at inspiration to simulate a patient treated at DIBH while still applying the cardiac waveform. The same plan may be delivered including respiratory motion to evaluate the avoided negative impact of respiratory motion in the delivered plan by comparing dose metrics between the configurations such as OAR sparing or PTV coverage.

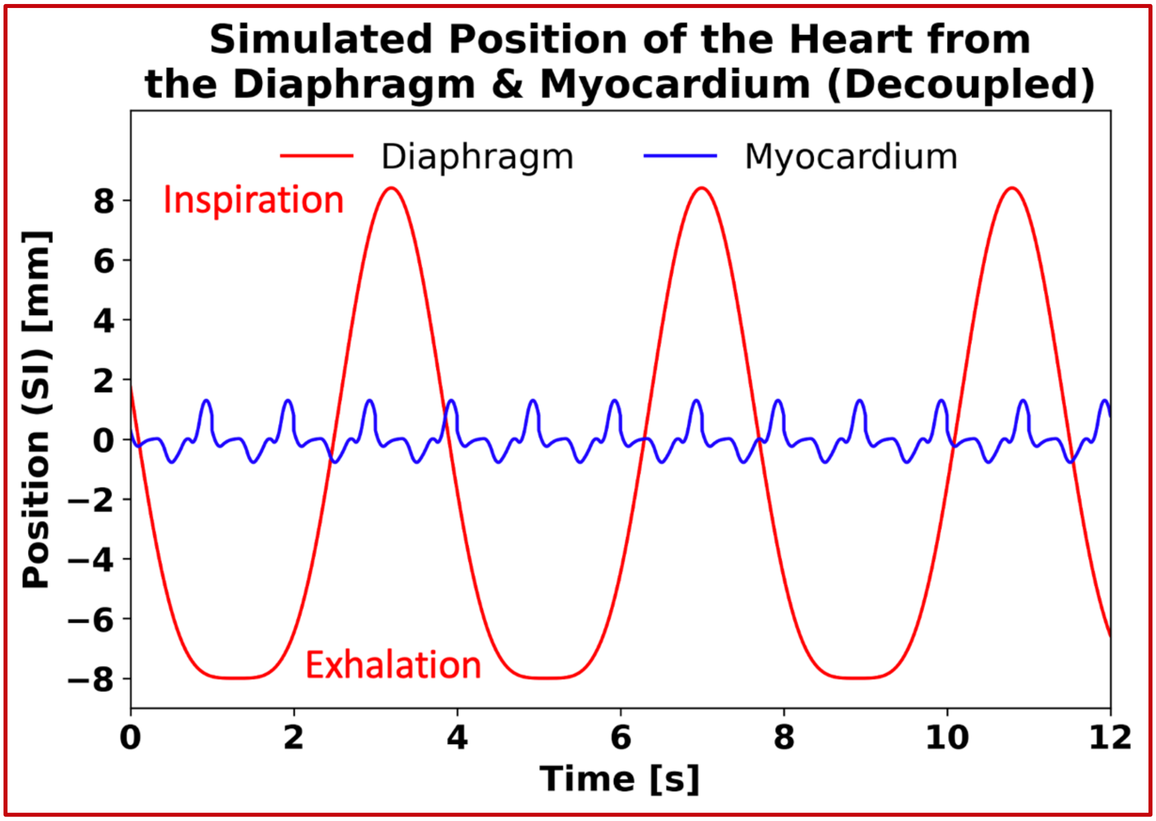

Figure 3. Approximated waveform of superoinferior (SI) motion given by diaphragm-induced $\cos^4$ waveform (red) at the patient average: 15.8 breaths per minute and amplitude 1.64cm. [28] Myocardium-induced motion [27](blue) occurs at 60 beats per minute according to the limitations of the MR-safe programmable motor.

To also incorporate out-of-plane motion, information from literature about the time-resolved twisting motion of the heart is also reported. Lorenz *et al* investigates the twisting motion of the heart from 0% to 80% systole in 10 healthy patients using cardiac tagged MRI. The twisting motion of the heart was found to be heterogeneous, varying from slice to slice moving from the base to the apex, with the maximum angular difference between these structures equal to 13°. [29] The high variability of twisting motion will be difficult to emulate in a rigid container design since the motor will apply rotation to the entire heart module, thus will implement an average twisting angle across all slices in each phase to produce a cyclic twisting motion profile for the motor.

2.3 Recent Advancements in Image-guided Radiotherapy

The introduction of CT to the radiation oncology workflow has revolutionized treatment planning, allowing medical physicists and dosimetrists to begin more complex 3D planning. Volumetric imaging provides a means to accurately identify and delineate internal target structures and OARs for optimized treatments in 3D space. Additionally, dose algorithms approximate attenuation of the treatment photon beam through internal tissues by using the patient-specific 3-dimensional spatial distribution of CT number mapped to the electron density for human tissues to enable accurate dose calculations. 3D planning, immobilization devices, and online adaptive radiation therapy (ART) allow for the precise targeting of lesions in stereotactic radiosurgery (SRS) and stereotactic body radiotherapy (SBRT) applications.

For positioning these patients in precise alignment of the radiation beam for these workflows, online imaging has become part of the clinical standard workflow. Today, cone-beam computed tomography (CBCT) can be found as an implementation on standard linacs. While CBCT systems provide good alignment for highly attenuating bone and fiducial markers, they fail to resolve soft tissue contrasts useful in abdominal cases. CBCT also uses ionizing X-ray photons which will cause damage to healthy tissues with a high number of exposures. Additionally, CBCT scan times are lengthy, requiring about 1 minute for data acquisition. [30] Because respiration occurs on a shorter time scale, linac-integrated CBCT is insufficient to provide the needed temporal resolution for applications near the diaphragm or heart, and often results in motion artifacts. [30] To resolve the lackluster performance of standard CBCT protocols in thoracic RT, 4D CBCT acquisitions by retrospective respiratory gating has been used to visualize moving tumors. [30] The projected multi-modality phantom will be useful for evaluation of these 4D CBCT techniques.

The first MR-linac was approved by the FDA in 2017 and has been transforming the field of ART. MR-linacs allow for superior ART that can resolve soft tissue contrasts for OAR sparing, enable real-time gating, and enable feedback changes throughout treatment fractionations. Most recently, the field has been moving towards multi-planar imaging for single-isocenter multi-target gating and cardiac applications. With these exciting yet complex techniques emerging, quality assurance tasks for these treatments require advanced phantoms and dosimetry.

2.4 Review and Limitations of Similar Works

With the increasing complexity of radiotherapy planning and online imaging, there has been an increase in the need for advanced phantoms to simulate human anatomy. A literature search was completed that investigated anthropomorphic phantoms including anatomies of the heart or diaphragm produced for medical physics applications in the past 15 years (Table 1). The most relevant phantoms discovered have been included in this table and outline limitations to overcome with the novel anthropomorphic phantom design. The phantoms in the review were found to lack many heart substructures or accurate motion profiles which will be addressed in the completion of the novel anthropomorphic phantom described in this work.

Citation; Image	Brief Description	Similarities	Key Differences & Limitations
Morton *et al.* [31]	• Adaptation of the deformable Extended Cardiac and Torso (XCAT) phantom for testing an improved 5DCT protocol	• Complex, deformable motion capabilities • Cardiac substructures	• Virtual Phantom
Shrestha *et al.* [32]	• Age-scalable computational heart phantom with substructures using atlas data • Calculates dose to substructures retroactively to study late effects of cardiac toxicity	• Calculation of dose for cardiac applications • Cardiac substructures	• Virtual Phantom • No movement
Kortelainen *et al.* [33]	• Kuopio Cardiac Phantom • Cylindrical-hemispherical shape • Simulating respiratory motion in SPECT/CT systems	• Simulates respiratory motion • Imaged in CT	• Only respiratory motion • Lacking many heart substructures • Not MR-compatible
Tavakoli *et al.* [34]	• Stationary chest phantom made from Plexiglas • Heart, lung, and ribs were made of cork and Teflon to simulate tissue densities for dosimetry • Used TLDs to measure dose to the heart and lungs from breast RT	• Anthropomorphic; including heart, lung, ribs • Dosimetry-capable (TLDs)	• No motion • Unclear if the heart model included substructures • No real-time dosimetry readout

Citation; Image	Brief Description	Similarities	Key Differences & Limitations
Bolwin *et al.* [35]	• Wilhelm phantom has compartments for lungs, heart LV, diaphragm, liver • Mount for lesions, ion chamber, or plaques • Motion hydraulically powered • Phantom can be used in PET/CT/MRI, and for radiotherapy applications to study motion effects.	• Anthropomorphic; including LV of heart, lung, diaphragm, liver • Motion-capable (Hydraulic) • Dosimetry-capable (ion chamber) • Multi-modality (PET/CT/MRI)	• Limited motion controls • Lacking many heart substructures
Huang *et al.* [36]	• Moving heart phantom made of two inflatable balloons to simulate the motion of the left ventricle • ^{18}F fills the space between the balloons to provide motion artifacts in PET • A ventilator pumps air to simulate the heartbeat	• MR-compatible; multi-modality • Simulates myocardium-induced deformable motion	• Limited motion control • No respiratory motion • Not dosimetry-capable • Lacking many substructures
De Deene *et al.* [37]	• Handmade positive PDMS mold of the LV of the heart with a hydrogel inner cavity • Movement is controlled by an in-house hydraulic pump	• Deformable motion phantom • Simulates myocardium-induced motion • Dosimetry-capable • MR-compatible; multi-modality	• Motion without rotation. • Lacking many substructures

Citation; Image	Brief Description	Similarities	Key Differences & Limitations
Swailes *et al.* [38]	• Flow-based MR-safe phantom to simulate heart motion and blood flow • Respiratory motion enabled by dual-phase respirator • Cardiac flow controlled by hydraulic system and syringes	• MR-compatible; multimodality • Respiratory motion	• Limited motion control • Not dosimetry-capable • Lacking many substructures; 2-chamber flow model
Kee *et al.* [39]	• Silicone gel MRI phantom of LV • Driven by hydraulics with an optical feedback system to control translation, compression, and rotation of heart phantom.	• MR-compatible; multimodality • Deformable motion	• Limited motion control • Not dosimetry-capable • Lacking many substructures; only LV
Groen *et al.* [40]	• Moving flow phantom to study the accuracy of a few imaging modalities. • Incorporates ECG output for ECG-gated imaging modalities	• MR-compatible; multimodality • Simulates myocardium-induced motion	• Lacking many substructures; only LV motion • Not dosimetry-capable • No respiratory motion
Boutchko *et al.* [41]	• Describes construction of a torso phantom that mimics respiratory and cardiac cycles, decoupled by multiple motion controls. • Uses flow and varied materials to achieve twisting motion	• MR-compatible; multimodality • Decoupled cardio-respiratory deformable motion • Dosimetry-capable	• Lacking many substructures of the heart

Table 1. Results of a literature search containing heart phantoms from the past 15 years similar to the projected phantom.

3 | Preliminary Evaluations

3.1 User Needs and Design Goals

The first step in the design process is to determine the user needs which are used to develop design goals for the project. The precise needs of the project are outlined in an NIH grant to "Develop [a] Novel Multi-modality Cardiac and Respiratory 5DMRI Phantom." This aim includes collaboration with an industry collaborator to expand a commercially available Quasar^{TM} MRI4D (Modus Medical Devices Inc., London, ON) motion phantom to incorporate modules that will integrate both cardiac and respiratory motion. Aspects of the current motion system are to include oscillation, offsets, rotation, bellows, and a research version incorporating ECG traces with imported patient-derived data. Modifications to this phantom will produce simultaneous cardio-respiratory motion with an MR-safe ceramic motor. 3D-printed cardiac substructures from patient imaging data will be implanted in the module for the representation of potentially irregular cardiac substructures for excursion and tracking evaluations. While fulfilling these needs is necessary to the project, none are limitations but rather serve as a starting point for creating a phantom with flexibility of adding more features.

A list of 12 phantom design goals was produced based on identified needs in the field of Radiation Oncology applications by a board-certified medical physicist with potential for future applications in Cardiology, Interventional Radiology, etc. These initial design goals are listed below:

1. Phantom substructures must give ample CT contrast against water.
    a. May add CT contrast agent such as Calcium Hydroxyapatite
2. Phantom substructures must provide MRI contrast against water during a rapid acquisition technique in 0.35 T field (ViewRay)

   a. May add MR contrast agents such as Gadolinium or Manganese
3. The materials used to fabricate the heart model should be flexible, having an elastic modulus similar to the heart muscle (10-500 kPa) [42]
4. The phantom should be able to take and retain the form of the heart.
5. The phantom materials should be resistant to permanent deformation.
6. All phantom components must be water compatible.
7. The phantom's outer dimension should be less than 7.5 cm to fit the constraints of the Modus water tank bore. Otherwise: use a different water tank
8. The anatomy of the phantom should include at least 12 substructures:
   a. Left Ventricle (LV), Left Atrium (LA), Right Ventricle (RV), Right Atrium (RA), Ascending Aorta (AA), Pulmonary Artery (PA), Pulmonary Vein (PV), Superior Vena cava (SVC), Inferior Vena Cava (IVC), Left Main Coronary Artery (LMCA), Left Anterior Descending Artery (LADA), and Right Coronary Artery (RCA)
9. The phantom motion should resemble the kinematics of cardiac tissue
10. The phantom should allow for dosimetry of multiple locations throughout the phantom
11. The phantom materials should cause minimal radiation beam disturbance
12. The overall design should be flexible for multiple end uses.

Out of the above twelve listed design goals, eight design goals were deemed essential and developed for the project, listed in Table 2. The first four goals are heavily material-dependent and directly useable for the material specifications in the next section, whereas the latter design goals incorporate multiple aspects of the overall design.

Essential design goal number one states that the CT number of the material used to produce the heart model should be close to the CT number of the myocardium (~39 HU) [43] suggesting a similar electron density to heart tissue for dosimetry calculations in treatment planning. The 2nd requires the entire designed system to be MR-compatible, including that the material provides ample signal contrast against the water background and the motion source to not cause artifacts that reduce image quality. Design goal 3 requires the durability of the material and housing apparatus to be resistant to permanent deformation, cracking, or tearing so that the phantom can withstand many usage cycles. As the phantom must have a substantial water component for effective MRI, the phantom must also be water-compatible and capable of repeated submersion in water for multiple days of experiments.

Eight Essential Design Goals
1. CT number ≅ myocardium
2. MR-compatible
3. Durable
4. Insoluble
5. Heart-like kinematics
6. Anthropomorphic
7. Retrofit to clinical equipment
8. Dosimetry-capable

Table 2. List of eight essential phantom design goals.

Design goal 5 requires the phantom to move according to both cardiac and respiratory motions which involves selecting a material that may be capable of deformation for future designs while considering the maximum output force (20 N) of the motor. This also brings into consideration the requirement that the first rigid prototype should be light enough for effective movement by the MR-safe motor. The sixth goal is pulled directly from the user needs, which requires anthropomorphic design including fabrication of the heart substructures using 3D printing from patient imaging data for anatomical accuracy. The seventh design goal refers to the MR-safe ceramic motor currently in the UW clinic, and integration with this is also a part of the user requirements. The industry partner has developed software to allow for importing decoupled motion waveforms from both cardiac and respiratory excursion data. The phantom housing module must be designed to retrofit the motor attachment end to properly utilize their technology. The eighth and final design goal is an expansion upon the original user needs and involves the incorporation of cavities to allow for dosimetry within the phantom module. Specifically, the plan is to use MR-safe multi-point scintillation detectors that allow for real-time dosimetry readout.

3.2 Materials Investigation and Decision Matrix

The materials investigation began with a literature search of candidate materials for the cardiac phantom anatomical structure. While the user needs stipulate the use of a 3D-printed (3D-P) material, the preliminary investigation included non-3D-P materials to gain information on the viability of a mixed-material design. A particularly useful resource was a literature review published in 2020 which included many materials and their utility for phantoms in imaging and therapy applications. [44] The two non-3D-P materials chosen for the decision matrix were Polyvinyl Alcohol (PVA) Hydrogel and Calcium Sodium Alginate Fiber and the five 3D-P materials were Thermoplastic Elastomer (TPE), Silicone, Thermoplastic Polyurethane (TPU) 92A, Agilus30, and Elastic50A. The scoring for Elastic50A and Agilus30 were updated based on experiments performed during the completion of this thesis.

Material specifications were developed according to the design goals and assigned a weight of 1-5 according to their importance, with 5 being most critical and 1 being least important. CT number and MR compatibility including signal contrast to water were the two most important material specifications, both earning an importance level of 5. Heart-like kinematics was also important and was given a 4 due to this being a user requirement. The durability and water compatibility specifications were both ranked at a 3, while ease of fabrication was given a lower score of 2. The weighted importance of these specifications is also reported in the specifications criteria guide below (Table 3).

Scoring Criteria for Material Specifications						
Specification (Importance)	**Material Property**	**Scoring Guide**				
		5	**4**	**3**	**2**	**1**
CT Number (5)	**|ΔHU|**	< 20	[20, 40)	[40, 60)	[60, 80)	≥ 80
MR Compatibility (5)	**Contrast to Water**	High	--	Moderate	--	No Contrast
Kinematics (4)	**|ΔE| [Pa]**	< 1	[100, 500)	[500, 1k)	[1k, 5k)	≥ 5,000
Fabrication (2)	**Difficulty, Resources**	Easy, Internal	Easy, External	Intermediate, Internal	Intermediate, External	Difficult, Ext./Int.
Durability (3)	**Strain% at Break**	≥ 100	(100, 75]	(75, 50]	(50, 25]	< 25
	Yield Strain%	≥ 40	(40, 30]	(30, 20]	(20, 10]	< 10
Water Compatibility (3)	**Hygroscopicity**	Waterproof	Low	Medium	High	Dissolves

Table 3. A scoring criteria guide to rate materials of interest. This provides the weight of importance (1-5) for specifications while outlining the metrics used to score materials according to their material properties in the decision matrix.

To give scores for the CT number of each material, a literature search was conducted and the materials were compared to the average CT number of the myocardium ($HU_{myocardium} = 39$ HU) at 120 kVp. [43] The score was determined by calculating the absolute difference in the material's CT number ($HU_{material}$) at 120 kVp, from the myocardium

$$|\Delta HU| = \left|HU_{material} - HU_{myocardium}\right| \tag{2}$$

TPE obtained a score of 1 due to its rather high CT number (100-200 HU) reported in the literature.

The MR compatibility was scored based on whether the material would display contrast against the water background while also taking into consideration whether or not the material could safely be placed in the scanner. Any materials containing ferrous metal which may be attracted to the magnets would be automatically disregarded. PVA is similar in MR properties to human soft tissue [45] resulting in a rating of "5." Each other material was rated as a 5 as well because they would show signal contrast to water background in the MRI, still allowing for visualization of complex structures.

To evaluate whether kinematics will be close to the heart muscle in a deformable model, the difference between Young's modulus, a measure of stiffness, to that of the myocardium was used as a criterion. The Young's modulus of the heart ranges from 10 to 500 kPa from the start to the end of diastole. [42] While this is certainly not the only mechanical property to affect the overall motion of a deformable material, this is the most often reported value in technical data sheets and literature, and therefore the most reasonable to use for the decision matrix. The equation used in the calculation for the absolute difference of Young's modulus (E) to the myocardium is given below:

$$|\Delta E| = \left|E_{material} - E_{myocardium}\right| \tag{3}$$

Thermoplastic Elastomer (TPE) received the lowest score in this criterion due to its very high average Young's modulus of 204 MPa, [46] which is approximately 3 orders of magnitude higher than the modulus of the heart.

Ease of fabrication was difficult to score because this is more qualitative than the other evaluation metrics and is dependent on professional expertise. The two identified driving factors that would influence the ease of fabrication include how the material might be manipulated into the form of the heart, and whether access to this process on-campus or through external means was provided. Therefore, this criterion was separated into accessibility to resources and difficulty in fabrication to encompass both ideas and scored based on each of these factors. A low-scoring material in this category was Calcium Alginate due to this being a specialty bioprinting material that requires a multi-nozzle bioprinting system. [47]

Durability was evaluated using the yield strain and strain at break of the material. Strain at break is defined as the percent deformation when a material breaks or fails. The yield strain is defined as the percent deformation from the original position that the material will no longer return to its original shape. Calcium Alginate scored the lowest on durability due to its exceptionally low strain at break of 13%, indicating this is a brittle material that would fail quickly. [48]

The results from a literature review on these materials were organized into a decision matrix, shown in Table 4 below. PVA Hydrogel, TPE, Calcium Alginate, Silicone, TPU, and Elastic50A were evaluated using the material specifications, which were weighted on a 1 to 5 scale of importance according to user needs. Overall, 3D-P materials scored higher due to the superior durability and ease of fabrication of these materials over non-3D-P materials. Therefore, the next chapter will focus on further investigation and characterization of 3D-P materials for use in the novel phantom.

Material Specification	Importance (1-5)	Material					
		PVA Hydrogel [44, 45]	Ca Alginate [49, 48, 47]	TPE (3D-P) [50, 46]	Silicone (3D-P) [51]	TPU 92A (3D-P) [51]	Elastic50A (3D-P)
CT Number Approximating Myocardium	**5**	3	4	1	3	4	5
MR Compatibility	**5**	5	5	5	5	5	5
Heart-like Kinematics	**4**	4	3	2	3	3	5
Ease of Fabrication	**2**	2	1	4	4	5	5
Durability	**3**	2	1	5	5	5	4
Water Compatibility	**3**	1	5	2	5	3	3
Overall Weighted Score	**-**	**3.1**	**3.5**	**3.0**	**4.1**	**4.1**	**4.6**

Table 4. Several candidate materials were evaluated in a decision matrix. A high-valued score indicates better overall material selection.

4 | 3D-Printed Materials Imaging Characterization

4.1 Computed Tomography

Computed Tomography (CT) is a helpful tool for medical physicists in a radiation oncology clinic. Nearly all patients who will be treated in a clinic will first be imaged on a CT-simulator (CT-SIM) to obtain 3D information about each patient's anatomy. CT is especially useful because of the capabilities of mapping CT number to electron density to determine the approximate attenuation coefficient for radiation in treatments using a Linear accelerator (Linac) or Brachytherapy sources. CT-SIM has transformed treatment planning and allowed for higher complexity treatments using Intensity-Modulated Radiation Therapy (IMRT) which can spare doses to healthy tissue and deliver high doses to target structures. Due to the importance of a CT-SIM in modern treatment planning workflow, several 3D-P materials were tested to evaluate which would have CT number closest to myocardium.

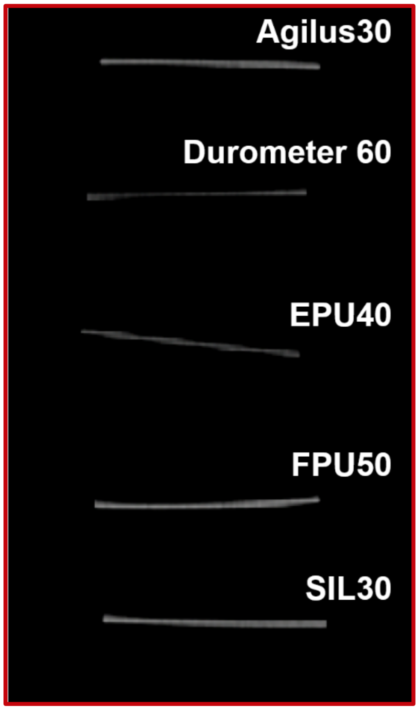

Figure 4. CT scan of five 3D-P materials; WW=400 HU, WL=40 HU.

A first batch of five 3D-P materials was supplied by Midwest Prototyping (Blue Mounds, WI) with the initial request requiring flexible materials using patient-informed design considerations for size with the width comparable to the lumen diameter of coronary arteries (~ 1.9mm at the distal LADA to the LMCA and an average of 4.5mm in healthy adults).[52] Strips (5x5x50 mm^3) of Agilus30, Durometer60, EPU40, FPU50, and SIL30 were obtained for testing.

The materials were imaged on top of a signal-generating phantom using a CT-SIM (Siemens SOMATOM Definition Edge) at 120 kVp. A coronal slice of the acquisition is shown in Figure 4 (0.98x0.98x2.0 mm^3). A small region of interest (ROI) for each test strip was contoured in MIM Maestro (Version 6.9.7; MIM Software Inc., 2022) for each material to estimate the average CT number. A thresholding value within ±40 HU of the estimated mean was used to guide auto-contouring of the sample strips. The CT number (mean ± standard deviation) from the ROI of each material are displayed in Figure 5. The number of voxels for the contours were ~300.

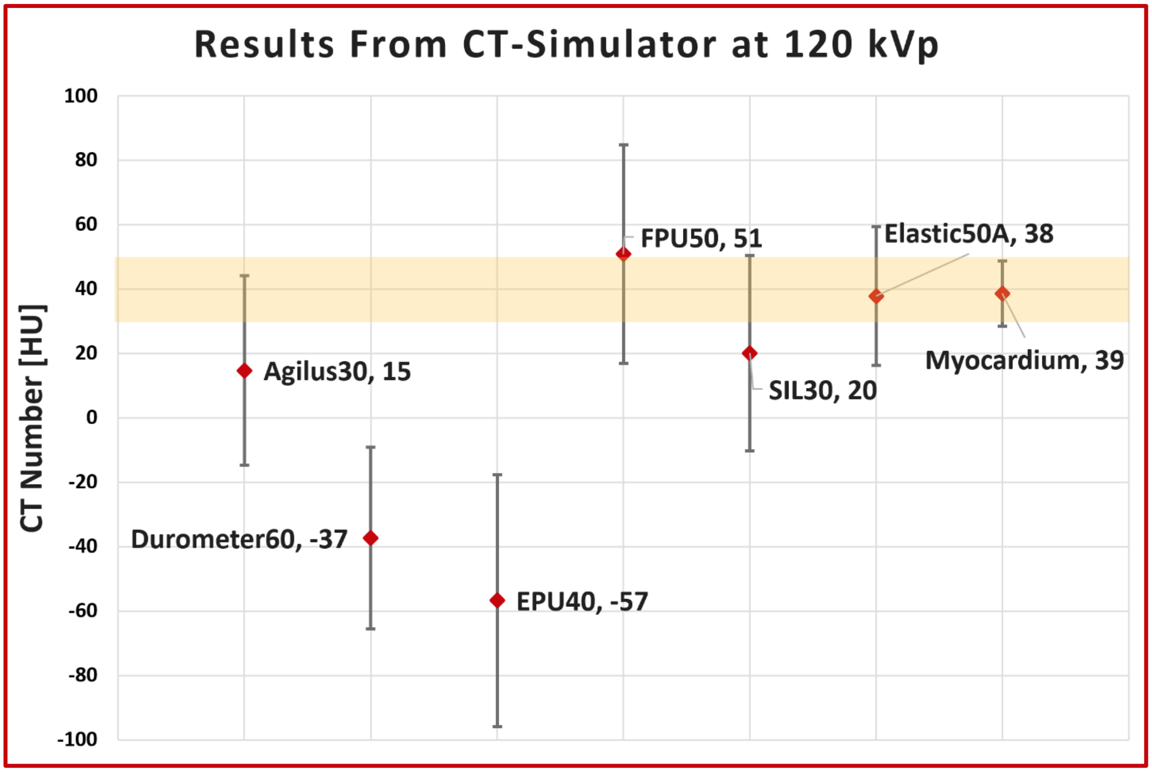

Figure 5. Scatterplot showing the average CT number of several 3D-P materials evaluated by contouring on a CT-SIM. Standard deviation (SD) is shown with error bars.

While the five samples from Midwest prototyping were chosen to be small to emulate the dimensions of a coronary artery, this may have affected the precision of the calculated CT Number of the material. Because the width and height (5x5 mm) of the five sample strips were larger than the voxel size (0.98x0.98x2.0 mm^3) of the CT-SIM, measurements of CT Number may be less precise than if larger dimensioned samples were obtained, as indicated by the large standard deviations shown in Figure 5. and these voxels which were contoured to obtain CT Number statistics may be affected by partial volume averaging. This phenomenon occurs at the interface of two materials of differing density occupy the same voxel, resulting in a volumetric averaged calculation of CT number for that point in space. While good approximations for the CT number of several materials were obtained, the results may have been skewed towards the CT number of the air background. Potential sources of uncertainty include material strips not being aligned well within a single axial slice, partial volume effects, and a low number of sample voxels from the contouring.

In the evolution of the research, additional resources were available via a Biomedical Engineering (BME) Design team at the University of Wisconsin–Madison, namely the use of a FormLabs Form 3BL 3D printer in the College of Engineering Makerspace. Alternative materials were identified that had low stiffness for potential deformable design, namely Elastic50A. A prototype 3D cardiac model was printed using Elastic50A to begin image testing. This printed model was also imaged in the CT-SIM to determine the CT number of Elastic50A (Figure 5).

4.2 Magnetic Resonance Imaging at 1.5T

While the Hounsfield Unit of water is, by definition, equal to zero for CT (and can be calculated theoretically using the mass attenuation coefficient of water), it is difficult to have such a metric for Magnetic Resonance Imaging (MRI). MRI signal comes from less fundamentally based interactions, and the voxel intensities may vary due to factors outside of the physical properties of the material. Even machines of the same manufacturer and model may produce different signal intensities of the same object due to the vast complexity of this modality. [53] The voxel intensities may vary due to field strength and properties of the gradient, differences in chosen acquisition parameters, protocols, sequences, or pixel sizes, as well as due to artifacts and variations in the signal-to-noise ratio. [54] Quantitative MRI including diffusion-weighted MRI, dynamic contrast-enhanced MRI, or T1/T2 mappings are often used for diagnosis although they are not readily integrated into MRI-guided radiation therapies. [55] As such, the magnitude of the signal generated from the materials is not what is used in the following evaluation, but rather the material detectability against a water background in common qualitative sequences used in radiation oncology—T1, T2, and steady-state free precession (TrueFISP) weighted imaging (Table 7). Since radiofrequency (RF) pulses in diagnostic MRI primarily target the Larmor frequency of Hydrogen atoms in water, while the materials may contain atoms capable of preferential alignment and net magnetization in the direction of the main field, they will likely not appear with any signal on diagnostic sequences due to their Larmor frequency being different than Hydrogen in water.

Field Strength (T)	Sequence	Acquisition $\Delta V_x/\Delta V_y/\Delta V_z$ (mm)	Bandwidth (Hz/ pixel)	α (°)	TR (ms)	TE (ms)	FOV (mm)
1.5	T1W	0.488 / 0.488 / 0.6	97.7	13	7.92	3.59	250 / 250 / 163
	T2W	1 / 1 / 1.4	195	160	12400	76.9	512 / 512 / 218
0.35	TrueFISP	1.5 / 1.5 / 1.5	534*	60*	3*	1*	399 / 432 / 399
	T2W	1.5 / 1.5 / 1.5	78**	90**	2000**	20**	400 / 228 / 264

Table 5. MRI sequence parameters for imaging experiments of 3D-printed samples. Axes x, y, and z indicate left-right, anterior-posterior, and superior-inferior directions respectively. *Parameters from Gach *et al.* [56]; **Parameters from Lewis *et al.* [57]

For quick and accurate image registration in radiation oncology workflows, the setup at the Magnetic Resonance simulator (MR-SIM) are the same as it would be in CT or on the Linac couch. For these data acquisitions, reproducible setup of the phantom for imaging on each modality and couch top was essential for the benchmarking and evaluation of several machines. When imaging the prototype heart model made of Elastic50A, the model was submerged in water to observe the signal difference to the water background (Figure 6).

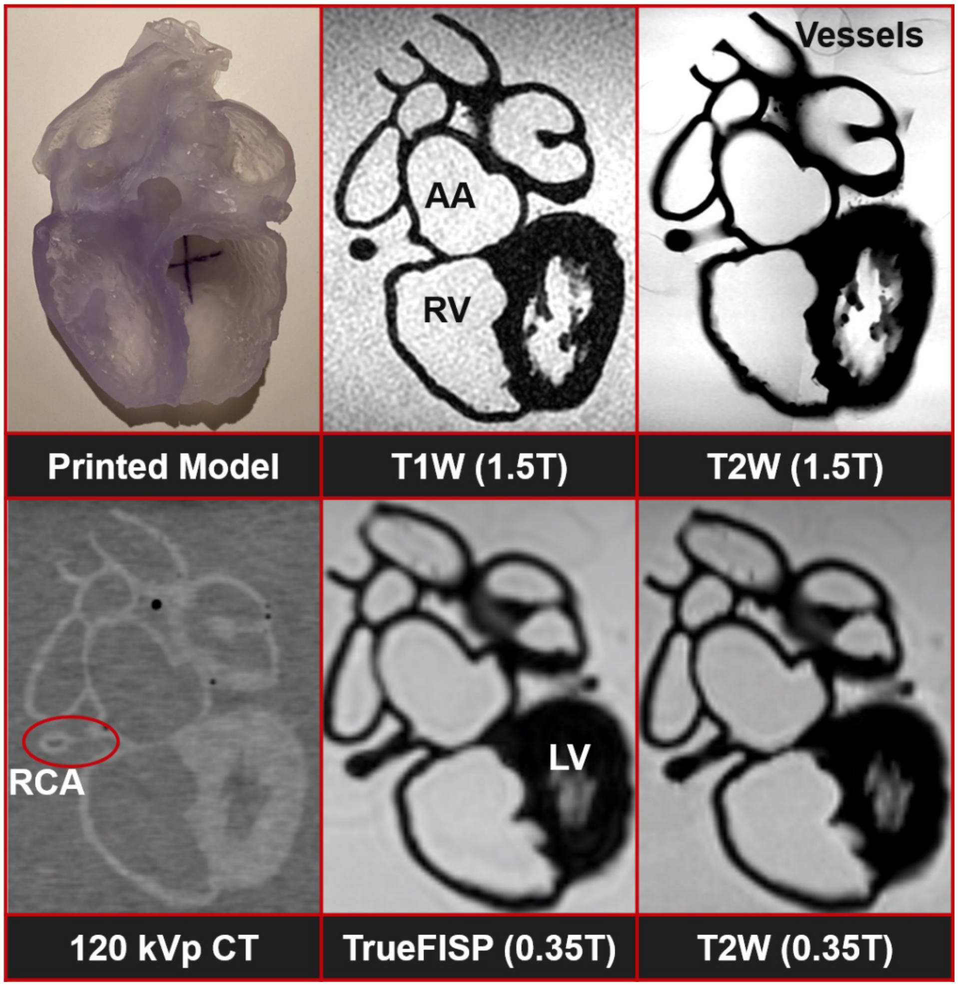

Figure 6. Prototype heart model with substructures visualized in several imaging modalities, labeled: Vessels, Ascending Aorta (AA), Right Ventricle (RV), Right Coronary Artery (RCA), Left Ventricle (LV).

4.3 Magnetic Resonance Imaging at 0.35T

MR images of the materials were acquired using true fast imaging and free precession

(TrueFISP) and T2-weighted sequences on a ViewRay MRIdian 0.35T MR-linac. As shown in Figure 7, all samples were successfully detected in 0.35T and the average signal was near-zero compared to water which produced a high amount of signal. Similarly, the prototype heart model was submerged to observe the material against water background and produced a near-zero signal against water.

4.4 Summary, Conclusions, and Limitations

The CT number of several 3D-printing materials was determined and compared to the heart muscle to determine which material most closely resembles the myocardium. MRI was performed at 1.5T and 0.35T to qualitatively verify that these materials could also be used to visualize complex heart anatomy against a water background. A prototype cardiac model was also 3D-printed to demonstrate the capabilities of a material to take and retain the form of the heart.

The best overall material used in this evaluation was Elastic50A, which was used to fabricate a prototype heart model for preliminary testing of this 3D-printing material for future fabrication work. The use of Elastic50A is predicted to satisfy the two modality-specific imaging design goals as well as the anthropomorphic design goal according to these experiments. Agilus30 and Sil30 remain good contenders for material choice if Elastic50A is incapable of fulfilling other design goals.

5 | Development of a Modular 3-Dimensional Heart Model

5.1 Computed Tomography with Coronary Angiography

Contrast-enhanced Computed Tomography with Coronary Angiography (CTCA) is commonly used in the clinic to evaluate the pathology of cardiovascular diseases affecting the coronary arteries. The contrast-enhanced CTCA scan was chosen due to the high spatial resolution (0.49x0.49x0.625 mm^3) over CT-SIM and MR-SIM systems, as well as the ability to differentiate between myocardium, coronary arteries, and blood volume over other imaging modalities. This information is critical to developing a patient-informed cardiac model that is anatomically accurate to fulfill the phantom design goals.

High-resolution de-identified patient scans of the heart were requested from the University of Wisconsin PACS database to contour and export a 3D cardiac model for research purposes. The image set contained several CTCA with contrast enhancement, and a single scan was selected based on the image quality, resolution, and cardiac phase. The CTCA scan chosen had been performed using a GE Medical Systems Revolution CT on an adult female patient in the feet-first supine position, with an approximate Body Mass Index (BMI) of 39, which is interpreted as obesity using the standard weight status category. [58]

Directly preceding the image acquisition, 100 mL of x-ray contrast agent was injected into the patient intravenously and the cardiac phase during acquisition was near-end diastole, with the nominal percentage phase recorded as 90%, and was obtained over a 0.35 second revolution time using proprietary software which determines an optimal time window near the nominal phase to minimize motion blur. The scan was acquired using 140 kVp tube technique in cine mode, resulting in a 256-slice DICOM image file with slice thickness and spacing equal to 0.625 mm. Each slice was 512x512 pixels with spacing 0.49 mm, yielding a high-quality scan for contouring.

5.2 Substructure Contouring and Model Preparation

Twelve heart substructures were contoured manually according to a widely employed cardiac atlas [59] on the contrast-enhanced CTCA scan using MIM Maestro (Version 6.9.7 and 7.2.8; MIM Software Inc., 2022) the standard clinical software used at the UW clinic for contouring in radiation treatment planning. The primary function of the cardiac atlas was to localize each cardiac substructure in the CT scan, as well as the superior and inferior borders of each substructure. A summary of the contoured substructures and their function are given in Table 6.

Classification	Substructure (Acronym)	Functional Role
Chamber Walls	**Left Ventricle (LV)**	Ejects oxygenated blood
	Left Atrium (LA)	Receives oxygenated blood
	Right Ventricle (RV)	Ejects deoxygenated blood to lungs
	Right Atrium (RA)	Receives deoxygenated blood
Major Vessels	**Ascending Aorta (AA)**	Carries oxygenated blood away from heart
	Pulmonary Arteries (PA)	Carries deoxygenated blood away from heart to lungs
	Pulmonary Veins (PV)	Returns oxygenated blood to heart
	Superior Vena Cava (SVC)	Returns deoxygenated blood to heart
	Inferior Vena Cava (IVC)	
Coronary Arteries	**Left Main Coronary Artery (LMCA)**	Supplies blood to left atrium and left ventricle
	Left Anterior Descending Artery (LADA)	Supplies blood to anterior left and right ventricles
	Right Coronary Artery (RCA)	Supplies blood to right ventricle and right atrium

Table 6. A summary of cardiac substructures [59] and their function.

The segmentation was completed by following an iterative design procedure involving four generations of contours. In the third generation of contours, an expert cardiovascular radiologist reviewed and provided guidance on how to improve the contours for anatomical correctness while also gave instruction on resolving overlapping contours for the modular substructure design. For example, the decision of whether the interventricular septum should belong to the left or right ventricle and gave focus on keeping the blood vessels intact. Physician input was incorporated into the final two iterations of the design.

After manual contouring, the LV was smoothed using the contour smoothing tool in MIM Maestro (Version 6.9.7 and 7.2.8; MIM Software Inc., 2022). While this method of contour smoothing worked well for the LV, every other heart substructure had walls that were too thin for smoothing. While the exact algorithm for smoothing in the software is unknown, if any contour was less than about 2mm in thickness, the smoothing operator would remove the contour from that thin region. For this reason, the remainder of the heart substructures did not undergo this smoothing operation. Instead, morphological operators were utilized for an effective smoothing operation. All contours were dilated (expanded) by 0.25cm followed by a 0.25cm erosion (contraction) step which is a well-defined process known as closing of a set in morphological mathematics. [60] This morphological closing operation reduced the total number of spurious regions created in manual contouring by closing narrow gaps and reducing thin spikes. This also filled the coronary arteries to make the model more conducive for 3D printing by reducing the number of support structures needed to fabricate the hollow and winding tubular geometry of the coronary arteries. Furthermore, the individual contours for the coronary arteries and major vessels were combined into a single contour to reduce the complexity of a prototype modular design for subsequent printing. The resulting contours are shown in Figure 7.

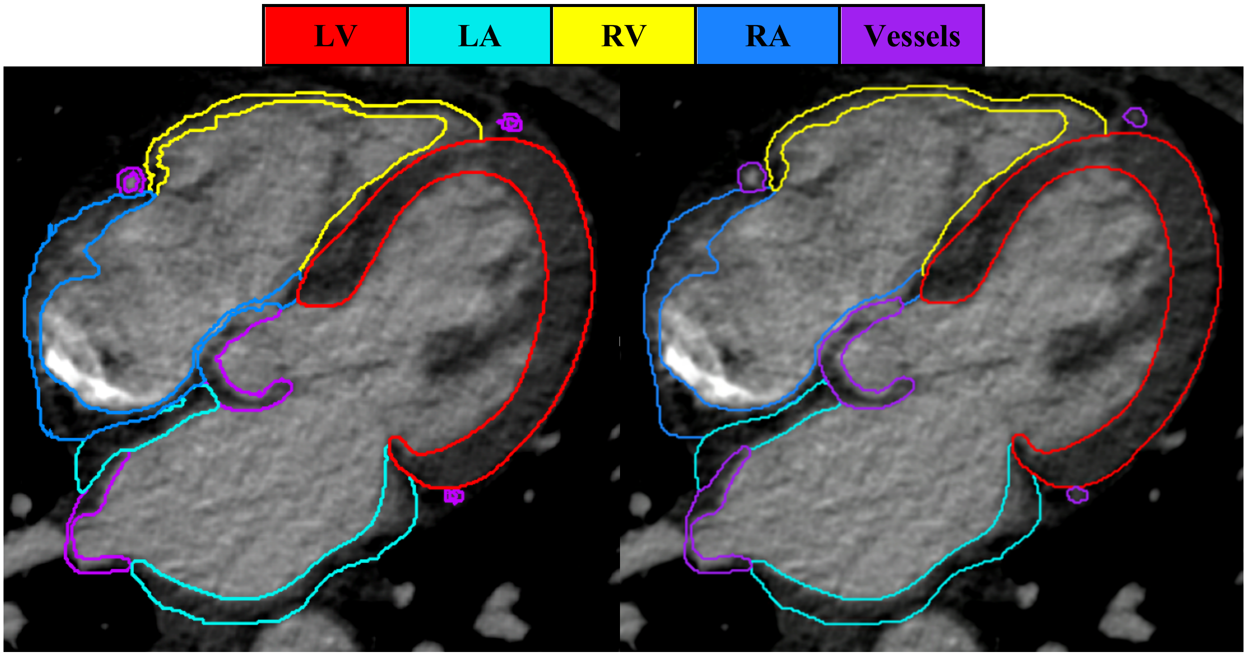

Figure 7. The fourth generation (v4) of heart substructure contours before and after the morphological closing operation. Labels correspond to Left Ventricle (LV, red), Left Atrium (LA, cyan), Right Ventricle (RV, yellow), Right Atrium (RA, blue), and blood vessels (purple).

Once segmentation work was completed on the CTCA scan, all contours were combined into one whole heart contour using the Union Boolean operator. This was followed by another morphological closing operation which connected the coronary arteries to the outer walls of the heart chambers, providing more stability during printing and contributing to the durability of a final printed model (Figure 8). Then the final step before exporting involved filling all holes volumetrically and removing all zero-volume contours. This effectively removed unwanted air pockets and removed floating single-slice contours that are not connected to the main model. Then, the ‘Export STL File’ built-in function was used to produce a 3-dimensional model of the whole heart which can be printed using Elastic50A.

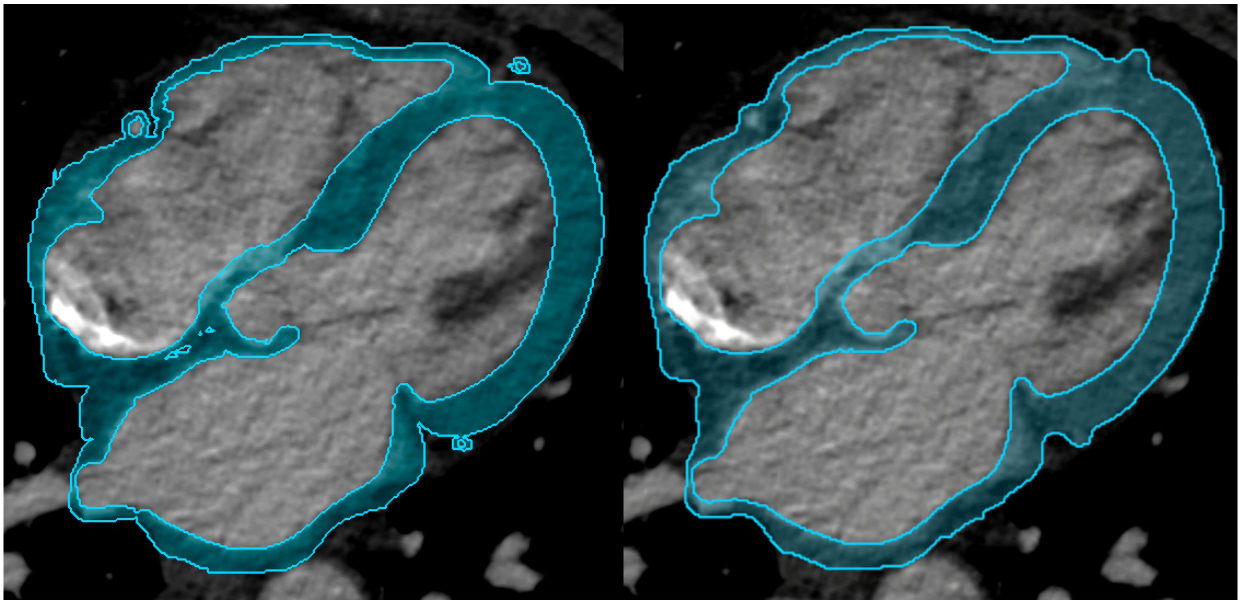

Figure 8. The left panel shows the manually drawn whole heart contours (v4) and the right panel shows these contours in the same slice following the closing operation, yielding v4-2.

The morphological closing operation completed appears to have the net effect desired by reducing spurious regions and narrow gaps in the heart contours. To evaluate the resulting change in contours from the original due to the operation, the Dice Similarity Coefficient (DSC, Equation (4)) was calculated using the manually drawn v4 whole heart contours (Figure 8) as ground truth and the v4-2 contours for comparison. The DSC for these two sets was calculated as 0.9142. Recent studies in novel AI heart segmentations indicate DSC between expertly manual-drawn whole heart contours of may be in the range of 0.9-0.96 with an average of 0.94. [61] This suggests the closing operation did not degrade the quality of the heart model past what would be acceptable between two sets of manually drawn contours reported in literature.

To evaluate the effects of the closing operation further, difference maps were evaluated between the two contour sets, and volume differences were calculated for each set of contours (Table 7). Overall, the operation resulted in a net gain of 18.87 mL.

Volume of v4 [mL]	Volume of v4-2 [mL]	Volume Added [mL]	Volume Removed [mL]	Net Volume Gained [mL]	DSC
345.07	363.94 (105.5%)	19.6 (5.7%)	0.74 (0.2%)	18.87 (5.5%)	0.9142

Table 7. Volumes from originial whole heart contours (v4) compared to volumes after morphological closing operation (v4-2). The operation caused a net positive gain in volume.

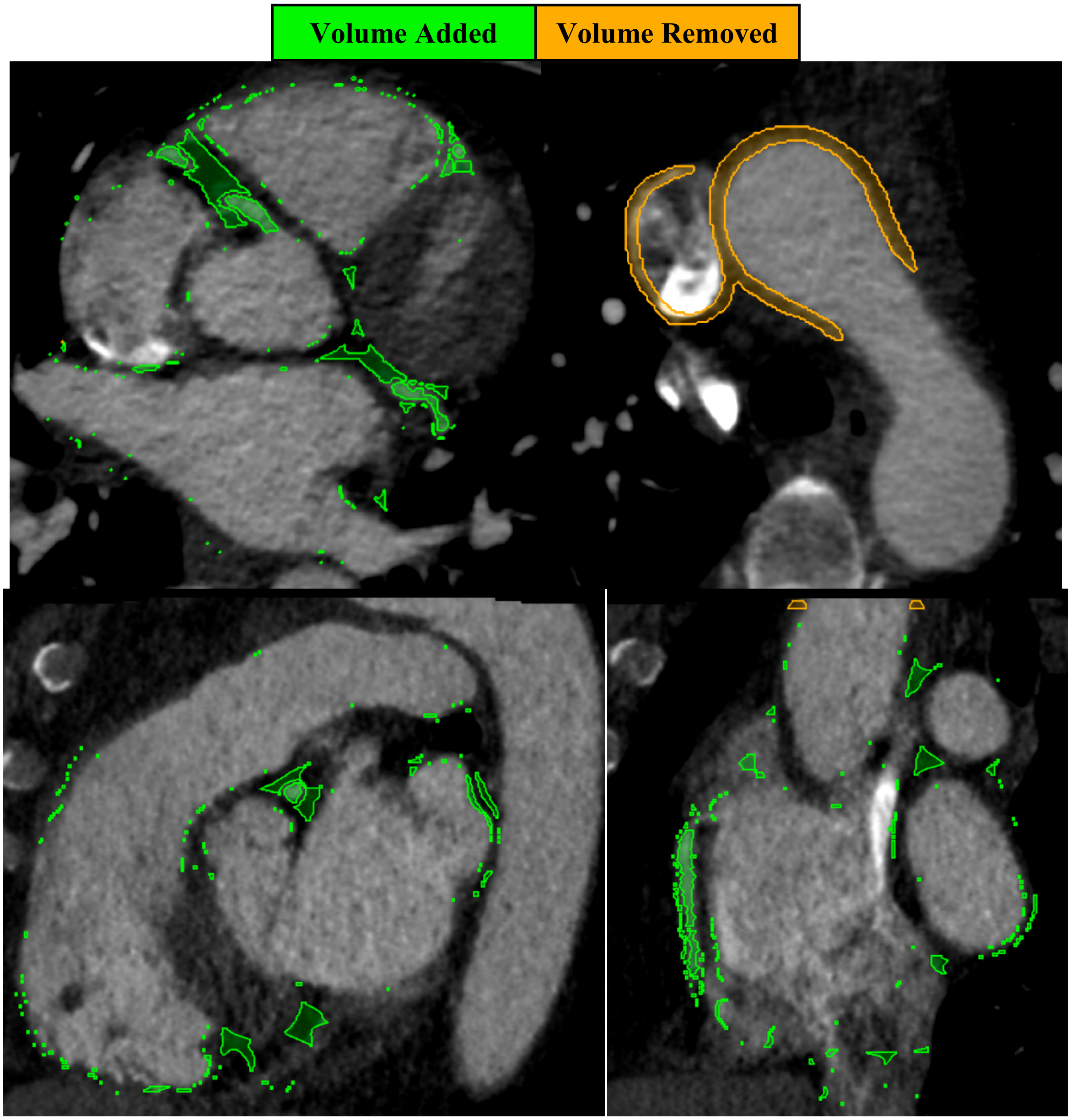

Figure 9. Difference map between pre- and post-closing operation in two axial slices (top) and two sagittal slices of interest (bottom). Subtracted volumes only appear in fringe cases, whereas volumes filled tend to be inside the coronary arteries and between substructures.

The difference map of these two contours aids in localization of changing volumes due to the closing operation (Figure 9). Much of the additional volume is coming from the filling of the coronary arteries as well as in the spaces between the chambers and blood vessels. Much of the volume removed was from the superior-most slices where the ascending aorta and superior vena cava abut the top slice of the image file. This removal is an unintended effect due to the inability of the contours to exist outside of the image in this software program.

While the morphological closing operations were effective at smoothing the contours within the resolution of the CTCA, the exported 3D model still appeared coarse due to the limitations of slice thickness and in-plane resolution of the CTCA scan. Therefore, the model was imported to Materialise Mimics (Version 23.0; Materialise NV, 2020) which can smooth the model with more fine resolution. A before and after rendering due to this post-processing step is shown below (Figure 10).

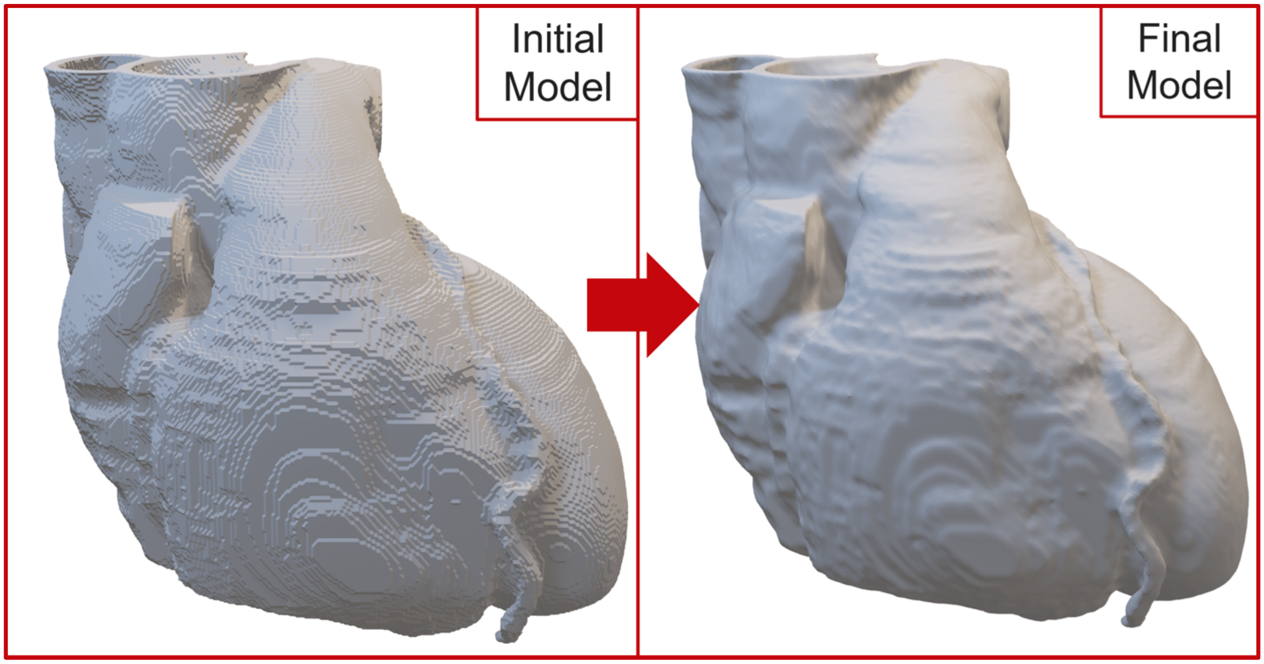

Figure 10. Fourth-generation before and after fine-smoothing step for the 3D heart model.

5.3 Model Evaluation

5.3a Model Smoothing

First, the exported STL and contrast-enhanced CTCA data were loaded into Mimics (Version 23.0; Materialise NV, 2020) and overlayed for visual evaluation of the smoothing procedure for manually drawn contours before the closing operation. The software utilizes the Taubin smoothing algorithm which specializes in surface smoothing without causing shrinkage, which is particularly useful for medical applications. [62] In this initial trial of smoothing, the smoothing operation was tested to observe if it would alter any features of the heart including topology of the coronary arteries, cause a reduction of wall thicknesses, or result in overall inflation of the contours.

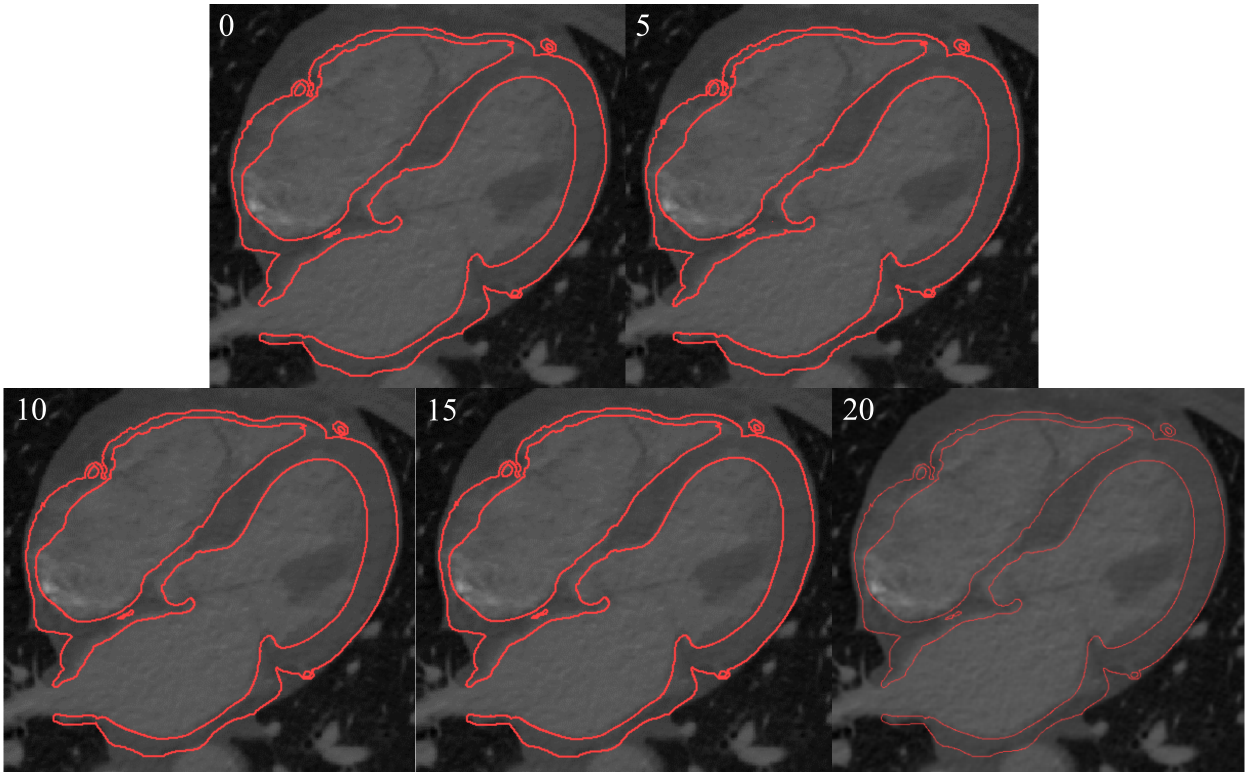

Figure 11. Results of contour post-processing in Mimics with 5-20 smoothing iterations.

There is an expected trade-off between model integrity and the degree of smoothing for 3D models. In general, the Taubin smoothing algorithm tends to accentuate spikes and holes, resulting in more spurious model surfaces which would not represent the original patient anatomy well. Collaborations with another lab who provided access to this software suggested using a smoothing factor equal to 1 for 10-15 iterations to avoid spurious surfaces and maintain the original model geometry. Therefore, 5, 10, 15, and 20 smoothing iterations were tested with this smoothing factor. Based on visual inspection, the contours still agreed very well with the unsmoothed heart model and did not result in these spurious surface regions (Figure 11).

To ensure that each smoothing operation did not alter the model beyond what may be acceptable, Dice Similarity Coefficients (DSC) were calculated for the fine resolution smoothing using a code developed in Python. The DSC is a measure of the volumetric overlap of two contours and is typically calculated using a computer-derived contour evaluated against ground truth contours. In this evaluation, the ground truth model is the original manually drawn 3D model (V_A), and the smoothed models are derivative (V_B). The formula to calculate DSC given two volumes is defined as double the intersection of those volumes divided by the combined volume

$$DSC = 2 \cdot \frac{V_A \cap V_B}{V_A + V_B} \tag{4}$$

The DSC for fine resolution smoothing in Mimics was evaluated in increments of 5 iterations with maximum of 20 iterations for a 3D volume against the whole heart without the closing operation (Table 8). The DSC was nearly equal to one in every case indicating that the Taubin smoothing algorithm does not significantly alter the morphology of the whole heart model. The overall integrity of the model was successfully held intact. This fine smoothing operation successfully reduced the coarseness of the initial model for 3D printing of a final prototype heart model using Elastic50A.

Iterations	**DSC**
5	0.9997
10	0.9997
15	0.9996
20	0.9996

Table 8. Summary of Dice Similarity Coefficient (DSC) for smoothing iterations in

5.3b Model Sizing

The overall diameter of the heart (~15 cm) was too large to fit within the possible diameter of the simulated module (~14 cm), so considerations were made to reduce the size of the overall model. The high BMI of the patient used for segmentation suggested that the derivative heart model may be larger than the size of an average adult male or female heart. [63] To quantify this, the LV of this 3D model was compared to published data from end-diastole LV myocardial mass (LV_M) evaluations in healthy subjects. [64]

The LV_M of the model was calculated using the wall volume established by the manually drawn contour multiplied by the specific gravity of the myocardium (assumed density $\rho = 1.055$ g/mL). The calculated LV_M of the contoured model using this method was 116 grams. This myocardial mass is in the 97.5th percentile according to the cohort of 381 healthy women aged 40-83. [64] This study also calculated the average LV_M indexed by subject height squared, which is 40. g/m^2 for the model and near the 97.5th percentile. The square of height is used as a surrogate for body surface area in the calculation of BMI and is used here to normalize the LV_M to the height of the individual.

Parameter	Contoured LV Model	85% Scaled LV Model	Reference Mean ± SD	97.5th Percentile
LV mass (g)	**116**	**72**	**85 ± 14** [64]	**116** [64]
LV mass/height^2 (g/m^2)	**40.**	**25**	**30 ± 5** [64]	**41** [64]

Table 9. Comparison of original and 85% scaled cardiac model to the reference left ventricular mass for healthy women (n=381).

To fabricate a prototype heart model closer to the LV_M of the average woman and to fit within the simulated module, an 85% scaled LV model was prepared and evaluated in Fusion360. The scaled model had a calculated LV_M and indexed LV_M within one standard deviation of an average healthy woman. This result suggests that the scaling operation resulted in a model size and volume close to that of a healthy woman.

5.4 Model Fabrication and Conclusions

The whole heart model was fabricated using Elastic50A on a FormLabs 3BL Stereolithography (SLA) resin printer. Since the printing process occurs layer-by-layer with increasing distance from the build-plate, structures with low-angled overhangs with respect to the build-plate tend to fare poorly without additional structures for adherence to other model components. Therefore, scaffold-like structures called support structures are commonly introduced to the model in preparing for 3D printing to increase print stability and integrity. Support structures also help with adhesion to the flat build plate and are particularly helpful for prints with rounded surfaces or small external faces. If support structures are not added to a complex-geometry print, there is an increased likelihood of failure. For these reasons, support structures were necessary to aid the fabrication process for the complex heart model (Figure 12, left).

Figure 12. Whole heart 3D-print on the build plate (left) and after post-processing (right).

The model was printed in 28 hours and 15 minutes after which the external support structures were removed. The model was then cured with ultraviolet (UV) light for 10 minutes and then washed in isopropyl alcohol for 20 minutes. Approximately 6 hours were spent in manual post-processing work of the printed heart to remove all external structures. This model was sent to an industry partner for engineering a stable mechanism to hold the heart within the volume of the first prototype heart phantom housing. Fabrication and engineering of the housing with this fixation mechanism are ongoing.

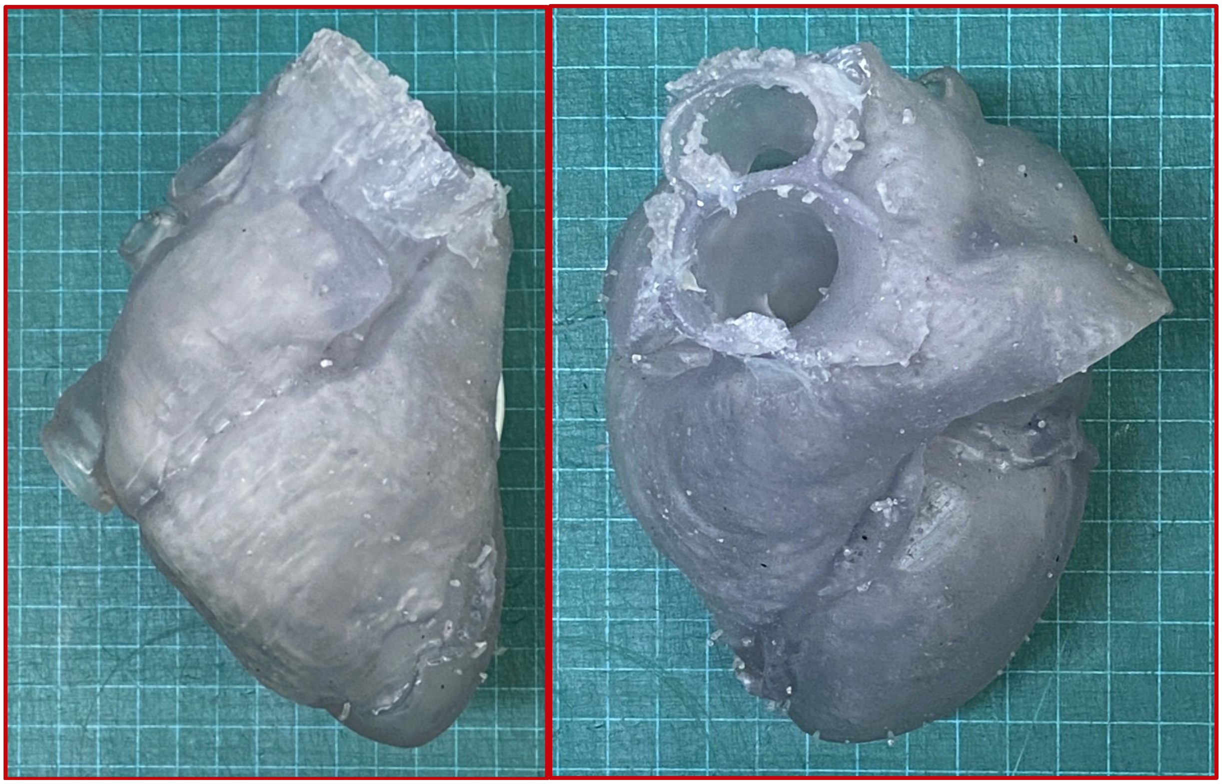

Figure 13. Two views of the fabricated heart are shown on a 1cm x 1cm square grid for size evaluation. The overall dimensions of the heart match the expected size.

Completion of the prototype model fabrication fulfills the anthropomorphic design goal for this project. Overall dimensions of the heart were taken to validate that the model was printed at the expected overall size of the original model. The overall model geometry was developed using a patient-informed design involving the contouring of heart substructures visualized in a contrast-enhanced CTCA scan. The design also included considerations for volumetric reduction of the heart to match the left ventricular mass of a healthy female heart.

5.5 Limitations and Future Work

While the cardiac atlas [59] includes several valves, these structures were not included in the initial development of the heart model as their inclusion would result in closed chamber geometries that would not enable water to filling in the chamber. Another atlas guideline [65] and novel segmentation methods [66] in radiotherapy applications do not apply segmentation to a visualized valve substructure but rather insert a disc-shaped region of interest where the valves are likely to exist based on known anatomy. This is due to the lack of the valves' prominence in images acquired via non-contrast CT. Overall, the decision to not implement valve substructures for this phantom will not significantly degrade the quality of the phantom for its intended use.

Another limitation of this work is that the final printed model was not imaged for comparison to the expected heart wall volume. This may be addressed in a future work that includes CT acquisitions of the final printed model followed by contouring for accurate volumetric comparison.

The high complexity of the heart model does not allow for easy access to the internal volume of the chambers where many support structures were generated. Therefore, many of the internal support structures remain inside the heart volume. The existence of these support structures may cause undesired effects on the morphology of the model in both CT and MRI, as they reduce the anthropomorphic qualities of the heart.

There are a few suggested pathways for the removal of these internal support structures. The first is to only allow the printer to create support structures on the build plate, thereby excluding all support structures originating on the internal surfaces of the model. This approach is not favorable since it will surely increase the risk of print failure. Another option is to carefully perform a partial dissection of the model after printing, remove the internal support structures, and glue the model back together. This would be a time-consuming task and compromise the integrity of the material, likely resulting in material failure.

A third, preferred option for the elimination of the internal support structures is to utilize the individual heart segmentation by exporting the contours for the blood vessels and four chambers as separate 3D models. By printing one at a time, the internal volume of each component will be more accessible for the removal of the supports. A secondary benefit to this method includes customization of materials for the several substructures of the heart to emulate tissue stiffness or CT number. This may help simulate motion interactions of individual substructures and visualization of substructures in the final design.

An alternative method for 3D-printing that could also eliminate internal support structures includes fused deposition modeling (FDM), opposed to the Stereolithography (SLA) method used for Elastic50A. A noted benefit of FDM is the high-durability and low-cost materials available for this method of printing, and the ability to use soluble support structures in this method. [67] These support structures are made of PVA and dissolves when a finished model is submerged in water, which removes the chance for destruction of the model in removal of support structures, and notable ability to remove support structures difficult to reach inside the FDM print. [67] However, the precision of FDM may be limited, and desired low stiffness materials may be difficult and less reliable to print in FDM when compared to SLA. [67]

Considerations for utilizing the segmentation of the cardiac substructures into a second-iteration prototype heart model are in development. The next printed heart is projected to be made of five modular components including the four chambers of the heart and the blood vessels. The mechanism to fit these components together involves removing small holes from the model before their fabrication on a 3D printer. Either large sutures or male and female rivet connectors will be inserted through these holes for attachment to form a modular heart model. Small portions of the heart model would also be removed to make room for interchangeable dosimetry inserts that could be used for radiotherapy experiments.

This modular design would also provide superior flexibility for the projected phantom. In one iteration, all substructures of the heart may be used. If a particular experiment does not require all substructures, some may be intentionally excluded, and the critical structures fashioned in a customized configuration for imaging or radiotherapy experiments.

6 | Mechanical Evaluations

6.1 Material Compression Testing

Another future design iteration may include deformable motion with the superior end held fixed, and the motor providing compressive forces from the inferior direction. While tensile elastic modulus is reported on the material data sheet, [68] no information was found regarding the compressive modulus. Therefore, to characterize the mechanical properties of Elastic50A more fully, nondestructive compression testing was performed on a material testing system (MTS). Three Elastic50A sample cylinders (2cm height, 2.5cm radius) were printed on the same FormLabs 3BL printer used for the fabrication of the heart model. A total of eight compression cycles were performed by applying a constant displacement rate of -0.2 mm/s vertically onto the surface of the samples without permanently deforming the materials (Figure 14).

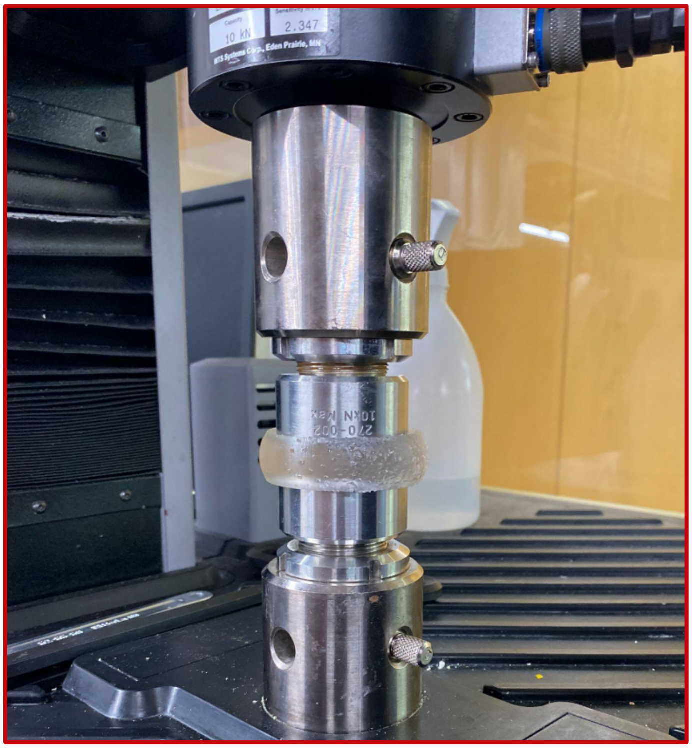

Figure 14. Compression of an Elastic50A sample cylinder on a MTS

The reaction force (F, N) as a function of time (t, s) reported by the MTS was used to calculate stress (σ, MPa) using the known cross-sectional area (A, mm^2) of the cylinders using the equation below

$$\sigma(t) = \frac{F(t)}{A} \tag{5}$$

Strain (ε) is a dimensionless quantity expressed in units of mm/mm or percent. This was calculated by using the displacement (x) of the head of the MTS at a given time (t) from the initial point of contact (x_0) and the original height of the material (h) defined by the following equation

$$\varepsilon(t) = \frac{x_0 - x(t)}{h} \tag{6}$$

When loading the samples on the MTS, the disks were placed in the center of the lower plate and the upper crosshead was lowered manually until just touching the surface of the sample disk. At the beginning of the test, an unknown number of data points were acquired which do not yield any meaningful results because the disk is not fully load-bearing, since the upper crosshead still must travel a small distance before initial compression of the whole disk occurs. This is attributed to fabrication defects such as warping or rashing resulting in the top of the sample disks not laying exactly parallel to the crosshead.

Therefore, to extract only the useful data from this test, the point of first full loading and compression was derived in the post-processing of the data and used as the true start of the test. First, the stress and strain values were calculated according to the equations above, and the slope between each successive value was obtained. A moving average smoothing of the slopes was utilized to reduce noise and observe the trend in slope over 9 data points at a time (4 prior values, 1 current value, 4 future values). Knowledge *a priori* suggests the data before full load-bearing accounts for a small proportion of the data, therefore the linear least-squares regression of the initial test data must have a slope that approaches the slope during the true test. Therefore, this slope was extracted for use as a thresholding value for flagging the beginning of the test. This threshold slope was compared to the smoothed slopes to determine the point of full load bearing for the Elastic50A disk. All data before the threshold value was removed for plotting and calculation of the compressive Young's modulus, or the stiffness of a material. The compressive Young's modulus (E_c) was calculated as the slope of the linear least-squares regression (Figure 15, 16) of the adjusted stress-strain curve for eight cycles according to Equation (7).

$$E = \frac{\Delta\sigma}{\Delta\varepsilon} \tag{7}$$

For comparison to the manufacturer-reported tensile Young's modulus (E_t), the value for stress (0.94 MPa) at 50% strain from the material data sheet was input to the defining equation for the calculation of a manufacturer-reported Young's modulus value. [68]

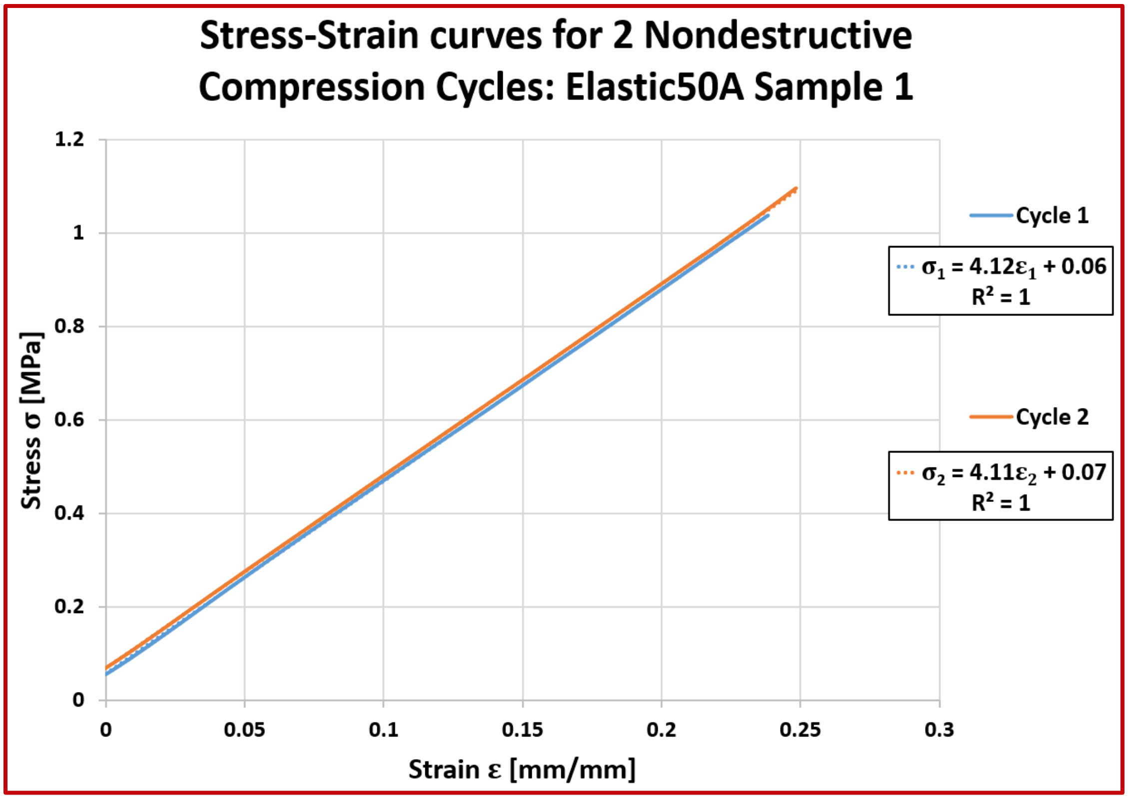

Figure 15. Calculated and graphed stress-strain curves (2 cycles) for Elastic50A sample 1 of 3. The slope of each linear least-squares fit is the Young's Modulus determined from a single cycle.

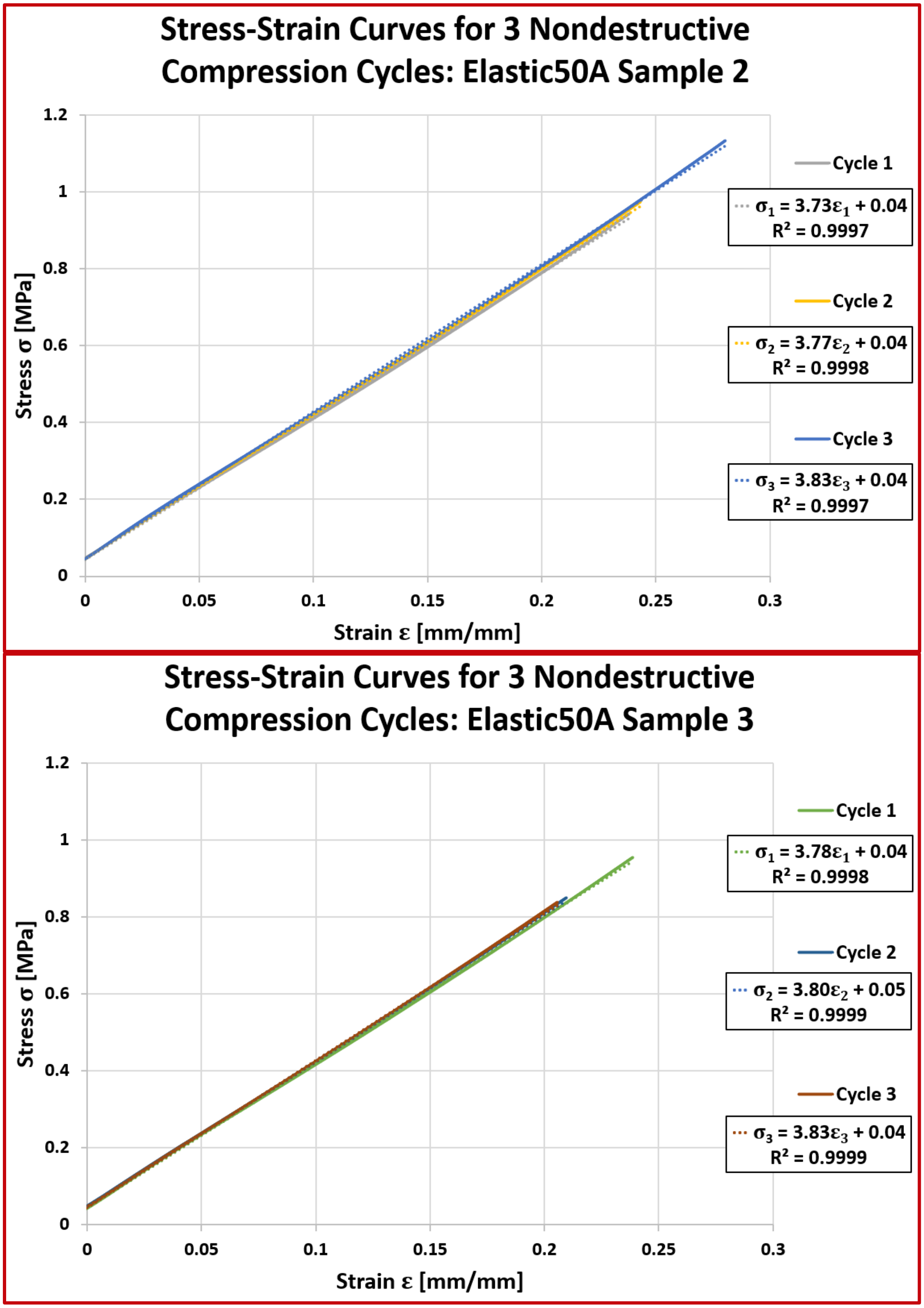

Figure 16. Calculated and graphed stress-strain curves for Elastic50A samples 2 (upper) and 3 (lower) undergoing 3 compression cycles each. The slope of each linear least-squares fit is the Young's Modulus determined from a single cycle.

Sample 1 (n=2) $\overline{E}_c$ ± SD [MPa]	Sample 2 (n=3) $\overline{E}_c$ ± SD [MPa]	Sample 3 (n=3) $\overline{E}_c$ ± SD [MPa]	Average Young's Modulus $\overline{E}_c$ ± SD [MPa]
4.12 ± 0.01	3.78 ± 0.04	3.80 ± 0.02	3.87 ± 0.14

Table 10. Average compressive Young's Modulus ($\overline{E}_c$) calculated for each sample of Elastic50A, then the average Young's Modulus across 8 total cycles was calculated.

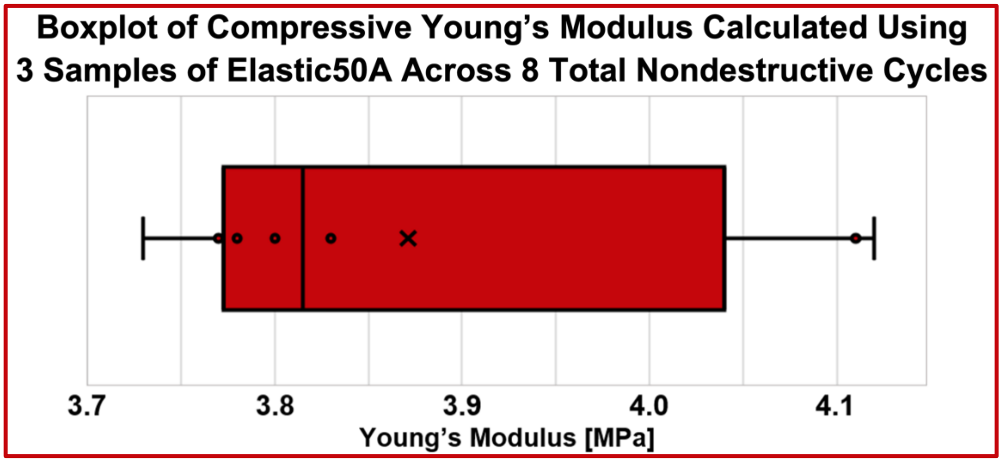

Figure 17. A boxplot summarizing the experimentally determined compressive Young's modulus for 8 non-destructive compression cycles using 3 samples of Elastic50A. The 'x' symbol denotes the average Young's Modulus across all cycles.

The average compressive Young's modulus calculated from the experiment was 3.87 ± 0.14 MPa, compared to the manufacturer-reported tensile modulus of 1.88 MPa for the same range of strains. Overall, the average results for the compressive are roughly double that of the manufacturer-reported tensile modulus. Based on findings reported by Li *et al*, 3D-printed plastics using SLA or FDM as a fabrication process should not be assumed to have isotropic elasticity. In SLA fabrication, this is due to the non-uniform curing of photosensitive resins resulting in parabolic microstructures according to the curing law of photosensitive resin. [69] Another 3D-printed plastic, ABS, was reported to have a compressive modulus roughly double that of the tensile modulus. [70] Based on these findings, the experiment yielded reasonable results when considering the class of materials tested.

The range of stiffnesses calculated from the 8 compression cycles was between 3.73 MPa and 4.12 MPa. The spread of values calculated for Young's modulus was fairly consistent for the compression cycles performed on an individual sample cylinder with the greatest standard deviation equal to 0.04 MPa indicating low intra-sample variation. The standard deviation of the entire group including all 3 samples and the combined 8 compression cycles was 0.14 MPa and indicates relatively high inter-sample variation. The largest statistical uncertainty from intra-sample variations was 2.1% (k=2), while the inter-sample variations increase this uncertainty to 7.2% (k=2) of the average value calculated. These results suggest that the cyclical loading of the samples was relatively self-consistent for a given sample disk and the fabrication process introduces a relatively larger uncertainty. The uncertainty of Young's modulus from the manufacturer is not reported in the datasheet, so the uncertainty is conservatively assumed to be 5% at k=1 for the experimental simulations completed in the next section.

6.2 Deformable Finite Element Methods

Now more information is known about the anisotropic properties of the material, it is now possible to determine whether the choice material Elastic50A is capable of deforming to emulate heart-like kinematics in next-iteration deformable motion design. To estimate the total deformation of the final cardiac model made of Elastic50A, computational evaluations were performed using ANSYS Workbench, a simulation software package that specializes in Finite Element Analysis (FEA). Deformable FEA determines model dynamics by breaking up a complex geometry into many smaller elements connected by nodes, the entire collection of which is called a mesh. A solution for the whole mesh is calculated based on the propagation of local node interactions informed by the elastic modulus of the material. The result is determined using numerical methods in a differential boundary-value problem. Boundary conditions are applied to elements, faces of elements, or single points to describe the system dynamics. The program is then able to calculate element stresses, strains, and total deformations based on the interaction between all the elements in the mesh. A static structural workflow project space was created in ANSYS workbench which contains 6 steps that require the user to define the (1) Engineering Data, (2) Geometry, (3) Model, and (4) Setup. From this, the program is then able to calculate a (5) Solution to the nodal displacements and forces and display them as user-specified (6) Results (Figure 18).

Two new materials were created first using the Young's modulus derived from the technical data sheet (E_t = 1.88 MPa). [68] The second input utilized the Young's Modulus from the experiment outlined in the previous section to create a linear isotropic elastic material emulating the compressive properties of the choice material (E_c = 3.87 MPa). The Poisson ratio for each of these materials was set to 0.3 to match the value for Elastic50A used in Tian *et al.* [71]

The geometry was imported to SpaceClaim from the final (v4-2) whole-heart model that was produced during the contouring step, before smoothing or scaling. After importing the model, the model was automatically repaired and defective faceted bodies were removed. Since this model is made of many surfaces, simplification of the model was necessary to satisfy program constraints not allowing for calculation of more than 100,000 nodes. Several simplifications were attempted with the Shrinkwrap feature starting at 2 mm and increasing by 0.5 mm increments. This parameter describes the largest distance between two surfaces that may be merged by this operation. Larger increments were attempted until a mesh with less than 100,000 nodes could be created with a 0.5 cm element size. This occurred at a Shrinkwrap setting of 4mm. The final simplified faceted model was converted to a solid body model merging all faces and moved to a new component. Then, the geometry was scaled uniformly in all directions to 85% of the original size. Scaling occurred after the Shrinkwrap operation to preserve the topology of the major blood vessels.

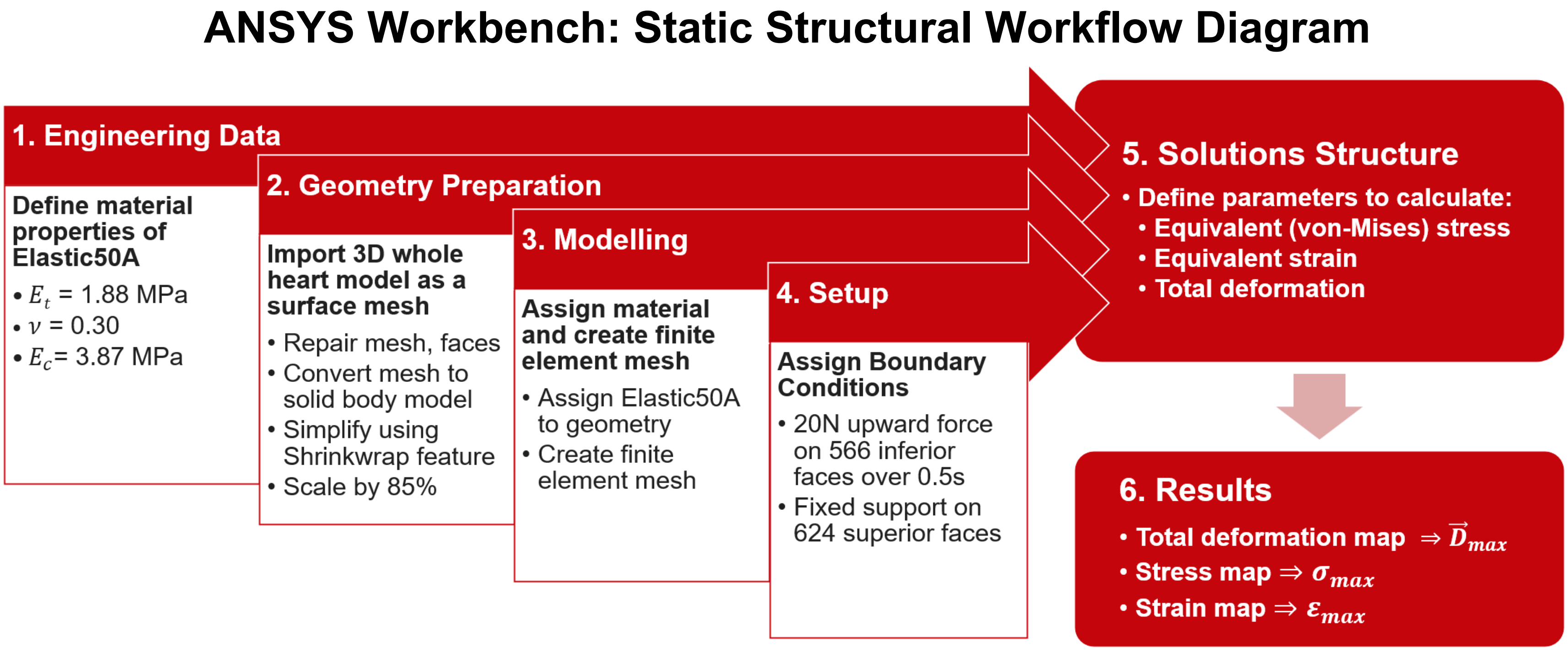

ANSYS Workbench: Static Structural Workflow Diagram

1. Engineering Data

Define material properties of Elastic50A

- E_t = 1.88 MPa
- ν = 0.30
- E_c= 3.87 MPa

2. Geometry Preparation

Import 3D whole heart model as a surface mesh

- Repair mesh, faces
- Convert mesh to solid body model
- Simplify using Shrinkwrap feature
- Scale by 85%

3. Modelling

Assign material and create finite element mesh

- Assign Elastic50A to geometry
- Create finite element mesh

4. Setup

Assign Boundary Conditions

- 20N upward force on 566 inferior faces over 0.5s
- Fixed support on 624 superior faces

5. Solutions Structure

- **Define parameters to calculate:**
  - **Equivalent (von-Mises) stress**
  - **Equivalent strain**
  - **Total deformation**

6. Results

- **Total deformation map** $\Rightarrow \vec{D}_{max}$
- **Stress map** $\Rightarrow \sigma_{max}$
- **Strain map** $\Rightarrow \varepsilon_{max}$

Figure 18. A workflow diagram describing the steps taken in the Static Structural deformable Finite Element Analysis using ANSYS Workbench. The project was broken into 6 tasks to simulate the stresses, strains, and deformations of a simplified model, then evaluated to find the maximum stress, maximum strain, and maximum deformation of a whole heart model made of Elastic50A in an expected design configuration.

Next, the modeling tab was utilized to assign the two Elastic50A materials using either the manufacturer-reported tensile modulus or the experimentally determined compressive modulus to the geometry. This is also when the finite element mesh is created from the solid body model. The physics preference, element order, and element size were set to mechanical, program-controlled, and 0.5cm respectively. The boundary conditions for the fixed support and force were applied, chosen according to a prospective future design where the ceramic motor would push with 20N of upwards force from the inferior direction while the base of the heart is held fixed (Figure 19). Finally, a total deformation, equivalent elastic strain, and equivalent (von Mises) stress were inserted into the solutions structure and a result was obtained in the calculation step.

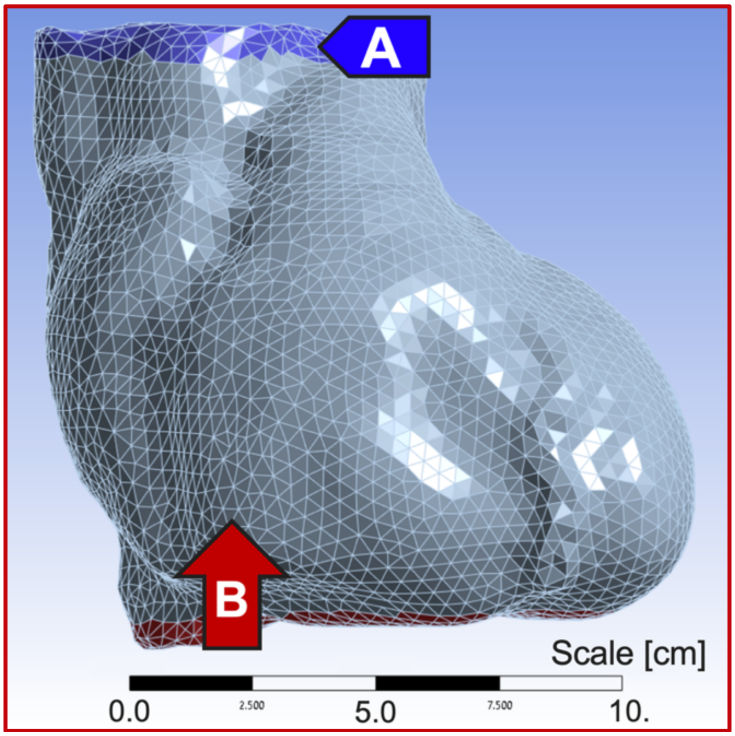

Figure 19. Boundary conditions applied to the heart model as a fixed support (A) on the 624 superior-most faces and a 20N force (B) on 566 inferior-most faces.

6.3 Finite Element Results and Analysis

Using the most recent cardiac model, deformable simulation results were obtained to verify the feasibility of a deformable phantom made of Elastic50A using the currently available clinical equipment. The heart is expected to deform up to a maximum of 0.91 ± 0.10 cm (k=2) [72] at the apex (Figure 20, left) using tensile Young's modulus reported by the manufacturer. [68] This value is greater than the centroid movement of the left ventricle at deep-inspiration breath hold (DIBH) reported in literature (Table 11). [27] These results imply that the LV of a whole heart phantom made of Elastic50A may be able to achieve motion goals at DIBH in a deformable design configuration using the MR-safe motor.

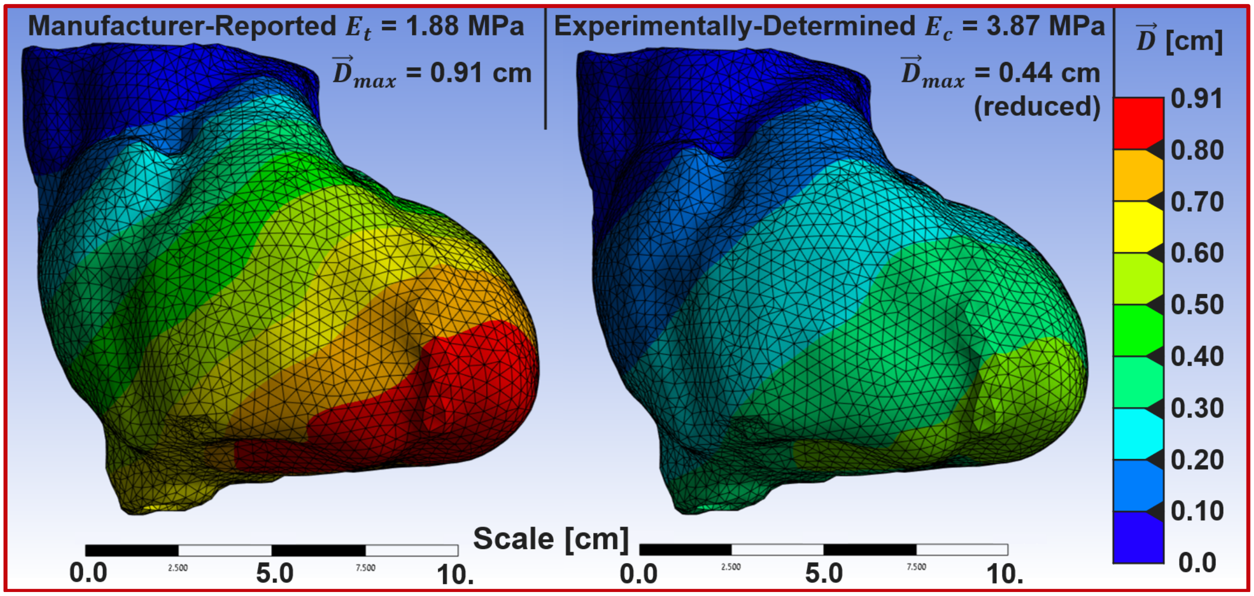

Figure 20. The FEA-simulated 3-dimensional total deformations ($\vec{D}$, cm) of the heart model using the manufacturer's specifications for tensile modulus (E_t) or the calculated compressive modulus (E_c). The maximum deformation is 0.91cm near the apex using the manufacturer-reported specification or 0.44cm using the experimentally-determined value.

However, since the loading applied to the model is compressive, applications of the initial simulation are limited by the assumption that the material exhibits the same mechanical properties under tension and compression. This does not appear to be the case based on the compression tests performed on the samples in prior sections indicating the anisotropic stiffness of Elastic50A. Therefore, the results from a simulation using the compressive Young's modulus were also considered. The total deformation of the model using the experimentally-determined compressive modulus is 0.44 ± 0.04 cm at k=2 [72] near the apex (Figure 20, right). This value is nearly half that of the deformation when using the tensile modulus, which is to be expected given the approximate doubling of stiffness. The results using compressive modulus are approximately equal to the centroid movement of the LV at DIBH [27] within the given uncertainty, suggesting the model will be capable of approximate LV movement without causing damage to the programmable ceramic motor.

To evaluate the performance of the material in this geometry, a mapping of the equivalent stresses and strains was calculated for the finite element model due to a 20N compressive loading using the two stiffnesses (Figure 21, 22). Using the manufacturer-reported tensile stiffness the maximum equivalent stress was found to be 289 ± 32.8 kPa (k=2) and the maximum equivalent strain was 17 ± 1.9% (k=2). Using the experimentally-determined compressive modulus, the maximum equivalent stress was found to be 289 ± 26 kPa (k=2) and the maximum equivalent strain was 8.3 ± 0.7 mm/mm (k=2).

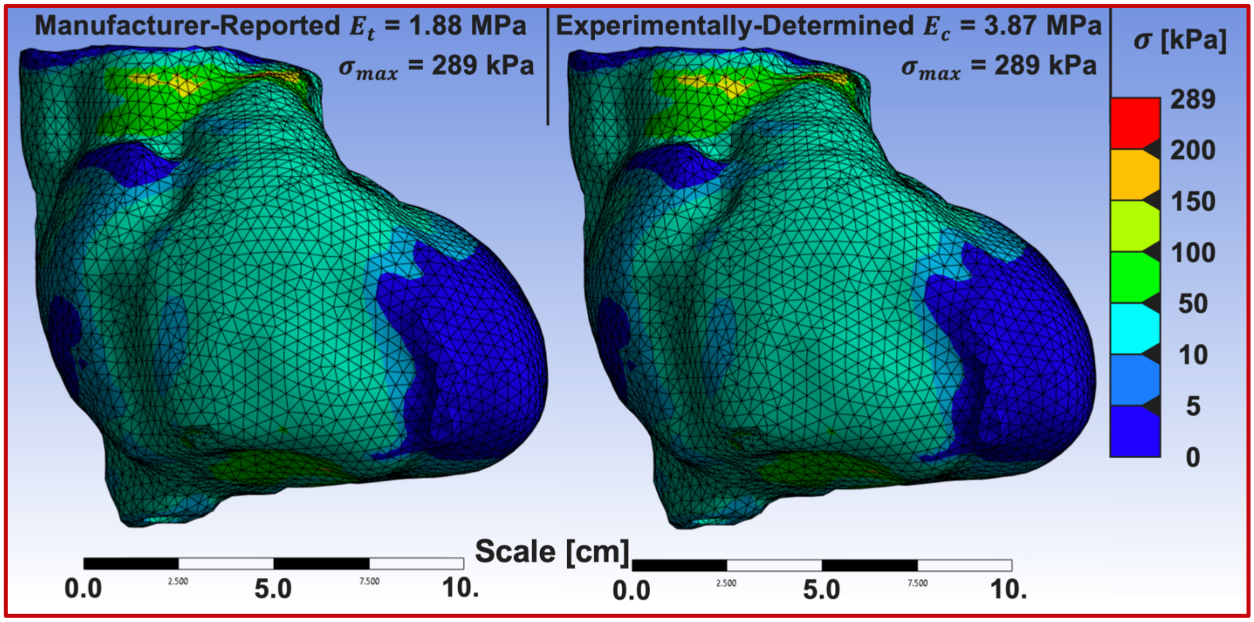

Figure 21. The FEA-simulated equivalent stress map (σ) of the heart model using the manufacturer's specifications for tensile modulus (E_t) or the calculated compressive modulus (E_c). The maximum stress is 289 kPa at the superior wall of the pulmonary trunk for each case.

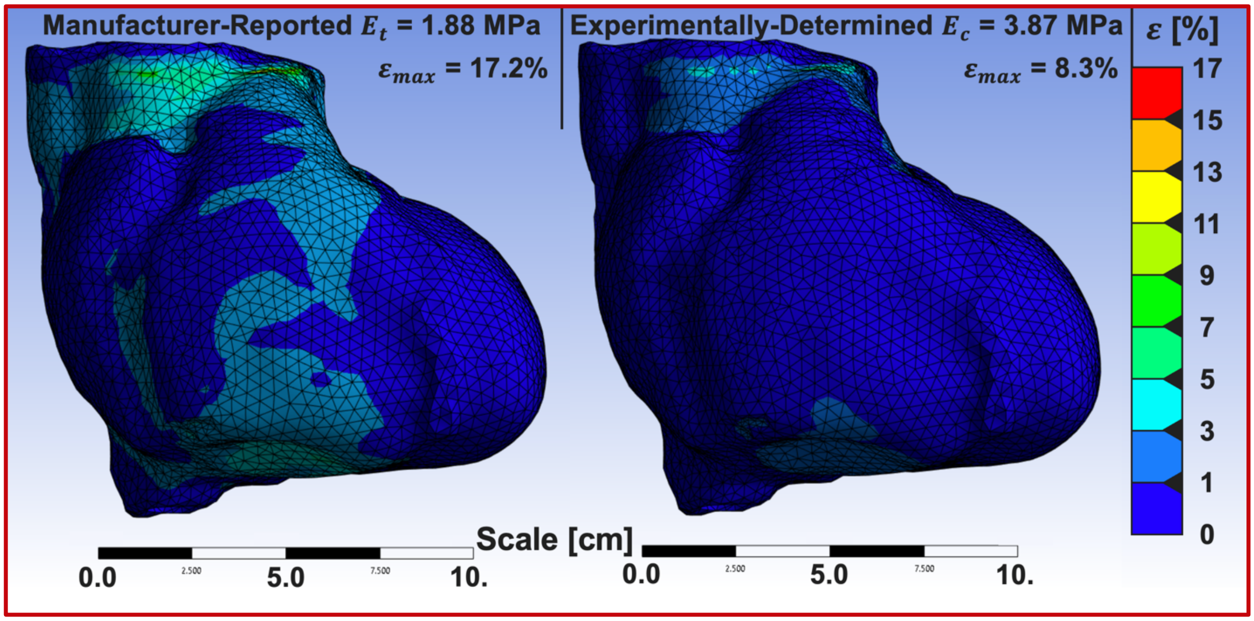

Figure 22. The FEA-simulated equivalent strain map (ε) of the heart model using the manufacturer's specifications for tensile modulus (E_t) or the calculated compressive modulus (E_c). The maximum strain is 17.2% at the superior wall of the pulmonary trunk using the manufacturer's specification or 8.3% using the calculated compressive modulus (E_c).

	$\vec{D}_{max}$ ± Uncertainty (k=2) [cm]	σ_{max} ± Uncertainty (k=2) [kPa]	ε_{max} ± Uncertainty (k=2) [%]
Result from Manufacturer-Reported E_t	**0.91 ± 0.10**	**289 ± 32.8**	**17.2 ± 1.9**
Result from Experimentally-Calculated E_c	**0.44 ± 0.04**	**289 ± 26.0**	**8.3 ± 0.7**
Threshold Value	**> 0.454** [27]	**< 3230** [68]	**< 160** [68]
Interpretation of Results	• Deformable phantom motion may mimic cardiac excursions • Verifies heart-like kinematics goal	• Model stress will not exceed Elastic50A's ultimate strength • Verifies durability goal	• Model strain will not exceed elongation at break • Verifies durability goal

Table 11. The maximal results from the simulated finite element analysis are given with uncertainty at k=2. The threshold value is given as the maximum centroid displacement due to cardiac motion of the LV at DIBH, ultimate tensile strength, or elongation at break.

In each simulation, the maximum stresses and strains occurred at the outer wall of the superior pulmonary trunk, adjacent to the simulated attachment point. The simulated maximum values of deformation, stress, and strain were summarized and compared to the ultimate tensile strength and elongation at break (Table 11) from the given material properties data. [68] These parameters became thresholding values to indicate the verified success or failure of the material in the simulations. The maximum simulated stress and strain values were found to be less than the threshold values, indicating the material will not fail in future deformable phantom designs using Elastic50A. In the case of failure, this break would likely occur at the outer wall of the pulmonary trunk according to the point of maximum stress and strain determined from this analysis.

Overall, the simulated results from the FEA given in Table 11 indicate a potentially successful deformable anthropomorphic design. Although the compressive modulus is not in the range of myocardium (10-500 kPa) [42], this simulation verifies the potential for Elastic50A to deform similarly to the left ventricle using the MR-safe motor. The simulation successfully verified 3 of the 8 design goals outlined for the project including heart-like kinematics, durability, and the ability to retrofit the motor based on the inputs and outputs of the simulations.

6.4 Conclusions, Limitations, and Future Work

The increase in standard deviation from intra-sample to inter-sample calculations suggests the 3D-printing fabrication process introduced additional variability, even for a simple geometry. Conceivable differences in the material include variations in density, overall dimensions, macro-scale fabrication defects, and internal microstructure defects, however, none of these were tested for directly other than the brief observation of macro-scale fabrication defects. Because the mass attenuation coefficient is normalized to the density of a material, high variations in density may affect the appearance of the model in CT and dose calculations when a 3D-printed model is used for radiotherapy experiments.

While the Poisson ratio was assumed to be 0.3 for the deformable simulations, an experimentally derived Poisson ratio should be calculated for more precise results. The Poisson ratio (ν) is defined as the rate of change of transverse strain (ε_{trans}) against the axial strain (ε_{axial}) expressed below.

$$\nu = -\frac{d\varepsilon_{trans}}{d\varepsilon_{axial}} \tag{8}$$

The Poisson ratio is a dimensionless quantity and useful for determining the shear modulus (G) when given the Elastic Modulus (E) according to the following relationship [72].

$$G = \frac{E}{2(1-\nu)} \tag{9}$$

In deformable finite element analysis, two out of three values in the above equation should be known to produce solutions to a model. These variables fully describe the stress-strain relationship for an isotropic and linearly elastic material resulting in convergence to an accurate solution. Using assumed values [71] of the Poisson ratio is sufficient for preliminary results, but future improvements would involve experimental determination of the Poisson ratio as well.

As concluded from the material compression testing, Elastic50A exhibits anisotropic mechanical properties. However, the simulations assumed a linear isotropic material which is due to a limitation of the material characterization. Overall, 3D-printed materials have much more complicated mechanical properties than can be determined by simple tensile or compressive testing. Characterization of these anisotropic materials in the simulation software requires knowledge of the symmetric 6x6 tensor containing stiffness or compliance values that fully describe the anisotropic properties of a material. Because not all the information necessary was available to appropriately describe the material in this manner, simulations were limited to those that assumed isotropic elasticity which was an acceptable assumption to approximate a range of values for deformation. Despite this limitation, a more scientifically rigorous simulation would require much more material testing for use in the simulation.

The simulated deformable model indicates that upon a single loading cycle of this heart model in the expected conditions, the material will not be loaded past the maximal strength of the material. However, many cyclic loadings may still cause material failure due to the initiation and propagation of microfractures in a process known as material fatigue. This experiment was unable to take into consideration the fatigue of the material over many cycles due to a lack of information about the cyclical loading of Elastic50A. In the future, cyclic loading tests of up to 50% elongation on several samples may be performed to evaluate the material fatigue of Elastic50A over the expected range of strains. Statistics from this experimental testing may also help indicate inter-sample variations at the microstructure level.

7 | Phantom Module Design

7.1 Interfacing with Clinical Equipment

To begin the design of the phantom module, several engineering drawings were obtained from the industrial partner depicting a standard insert and the standard hollow body oval. These engineering drawings were used to create 3D renderings of the clinical apparatus in SolidWorks for a complete understanding of how a new design might be implemented. The most critical aspects of the clinical phantom are the mechanical attachments to the ceramic motor to fulfill the heart-like kinematics design goal. This includes the dovetail interface on the front of the hollow body oval for holding the motor stable during motion as well as the finger clamp where the motor clasps onto existing phantom inserts.

The approximate inner diameter of commercially available phantom inserts is 7.2 cm and thus too small to allow for the insertion of the finished heart model with a width of nearly 12 cm. This necessitated design of a larger phantom insert and modified hollow body oval with a larger bored housing, all while maintaining the integrity of the interface between the motor and the insert. To reduce the overall cost of the phantom and expedite the manufacturing process, an existing prototype hollow body oval with a large bore of approximately 17.5 cm was used. While this prototype oval was large enough for the projected size of the heart module, there was no dovetail interface to enable the use of the motor with it this component.

As a solution to keep the process expedited, the front of an existing hollow body oval was proposed to be cut and placed on the front face of this large-bored oval (Figure 23). Four extension posts of 5cm in length were placed on a removable adapter piece to allow for the placement of dosimeters through the front of the oval. The space on either side of the front of the oval will allow for cords to feed through and back to readout devices in the control room.

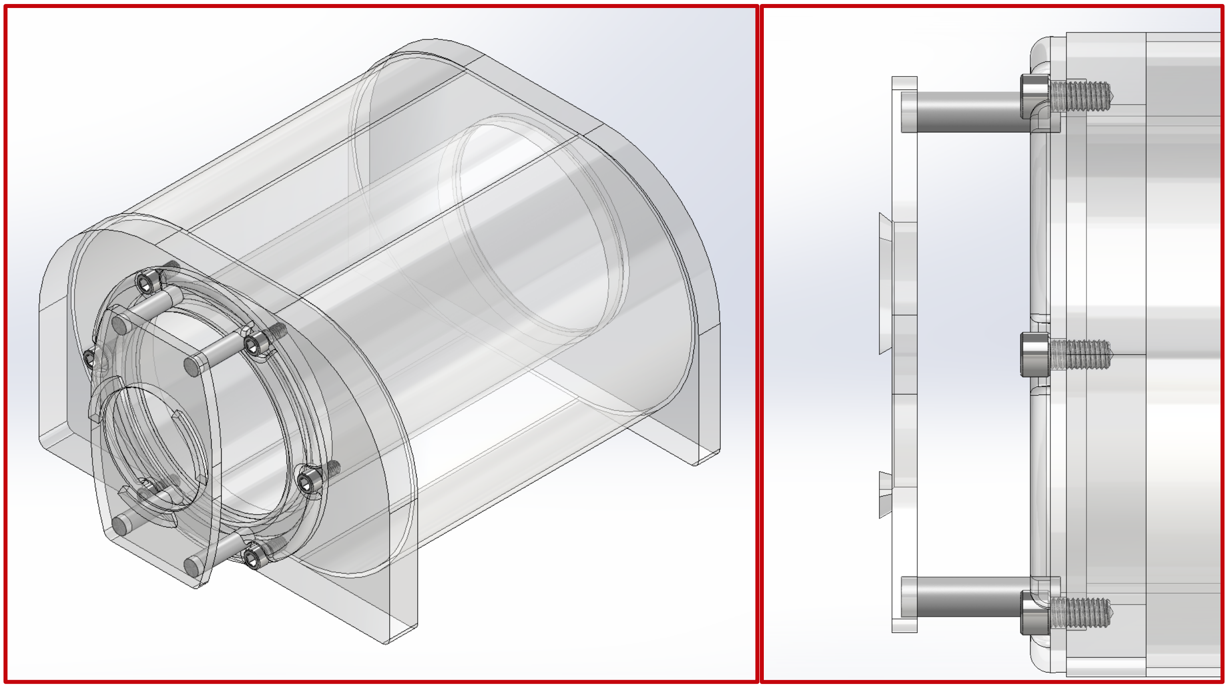

Figure 23. 3D-rendering isotropic view (left) of the modified hollow body oval with an adapter piece on the front face to attach the dovetail interface (right). This modified oval will allow for a larger cylindrical module to be inserted to accommodate the fabricated heart.

7.2 Features of the Novel Heart Module

The overall heart phantom module contains bulk model structures or fluids relevant to medical imaging including but not limited to CT, MRI, PET, or other imaging modalities. The first iteration of the design is specific to anthropomorphic heart anatomy, but this could be changed to simulate liver, lung, non-anthropomorphic structures, fluids with or without contrast agents, air, or other conceivably useful substances for medical imaging or radiotherapy applications. The bulk phantom model is capable of being removed and interchanged with different inserts depending on the purpose of the scan. Sealable fill ports for liquid-filling the phantom module or hollow body oval are included to enable MR imaging. The flexible nature of the overall design can allow for stationary uses or incorporate motion. In this implementation, the module will be attached to a ceramic motor for enabling motion during imaging using the long drive end of the module towards the right of the figure below.

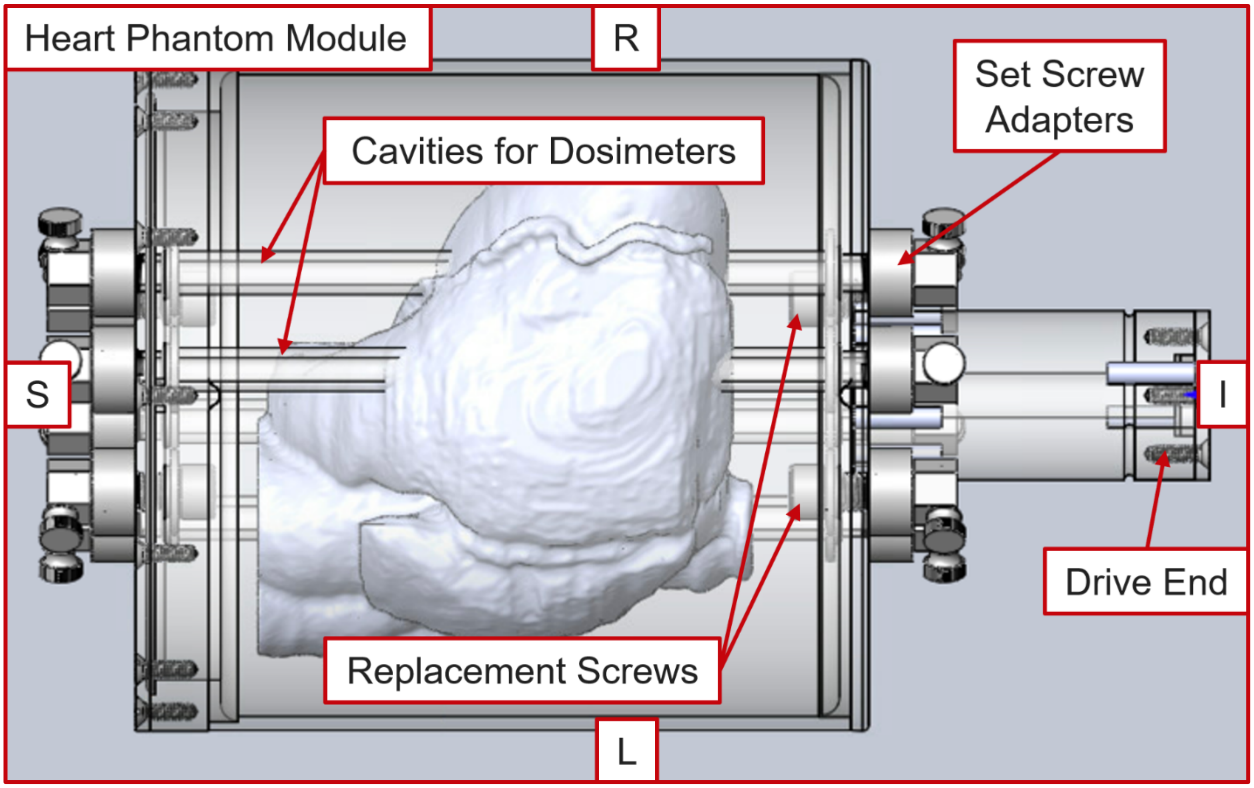

Figure 24. A CAD rendering showing the heart inserted to a rigid motion module and 4 cavity rods through the volume and heart to allow for the insertion of dosimeters. The drive end (right) retrofits to the MR-safe motor. Flexibility of the design allows cavities to be replaced by screws for many use cases. Directions are noted Left (L), Right (R), Inferior (I), Superior (S).

As shown in Figure 24, in its full implementation, the phantom module can receive up to 6 cavities that can hold dosimeters throughout the internal volume to obtain dosimetric readings during radiation therapy deliveries. These modular liquid-tight cavities can be inserted if needed or removed such as for MR-SIM applications via insertion ports on the phantom module surface utilizing a sealing mechanism. The cavities will be open to ambient air on at least one end and placed through the whole or partial interior of the phantom module.

These cavities allow for the insertion of any items of conceivable use in medical imaging or radiotherapy, including but not limited to contrast agents, tumor surrogates, dosimeters, fluid vessels, pacemaker leads, stents, sutures, other medical implants, metal fragments, or water-based gels. These items may be placed inside the cavities and indexed using known conditions for repeatable and predictable positioning of different items including dosimeters within the cavity. The location of the insertion ports for the cavities can be optimized based on the phantom anatomy to allow for targeting regions in and around the phantom for clinical relevancy. If an insertion port is not utilized by a cavity, flexibility is offered to remove this option by replacement with a screw (Figure 26).

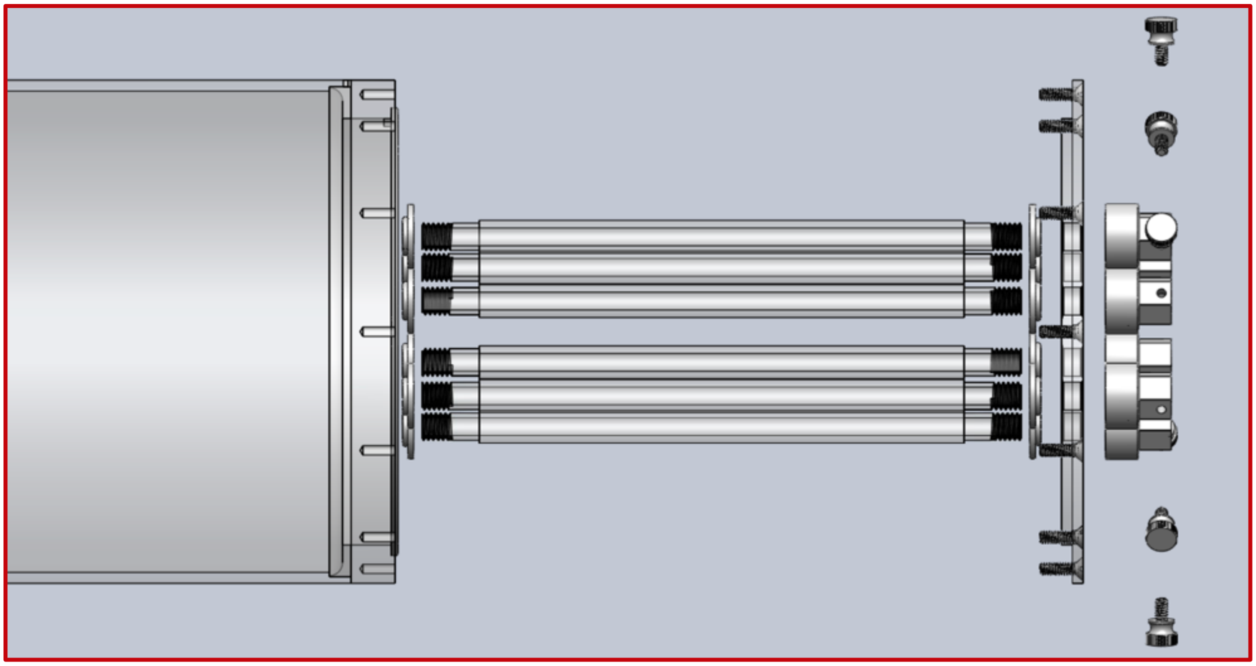

Figure 25. An exploded 3D rendering of the heart module showing the backplate and 6 cavity rods removed from the module housing. Rods can be used to insert measurement objects, needles, leads, etc., or not be used at all due to the modularity of the design.

The innovation of this phantom module is helpful and necessary for advancements in imaging, radiotherapy, and other settings. For medical imaging, there are often moving structures or fluids that are critical for the diagnosis of disease or precise localization needed for treatment planning of surgical interventions or radiation therapy. These cavity inserts allow for the placement of such items in a variable geometry phantom module for endpoints such as image quality optimization, target localization, and real-time motion tracking.

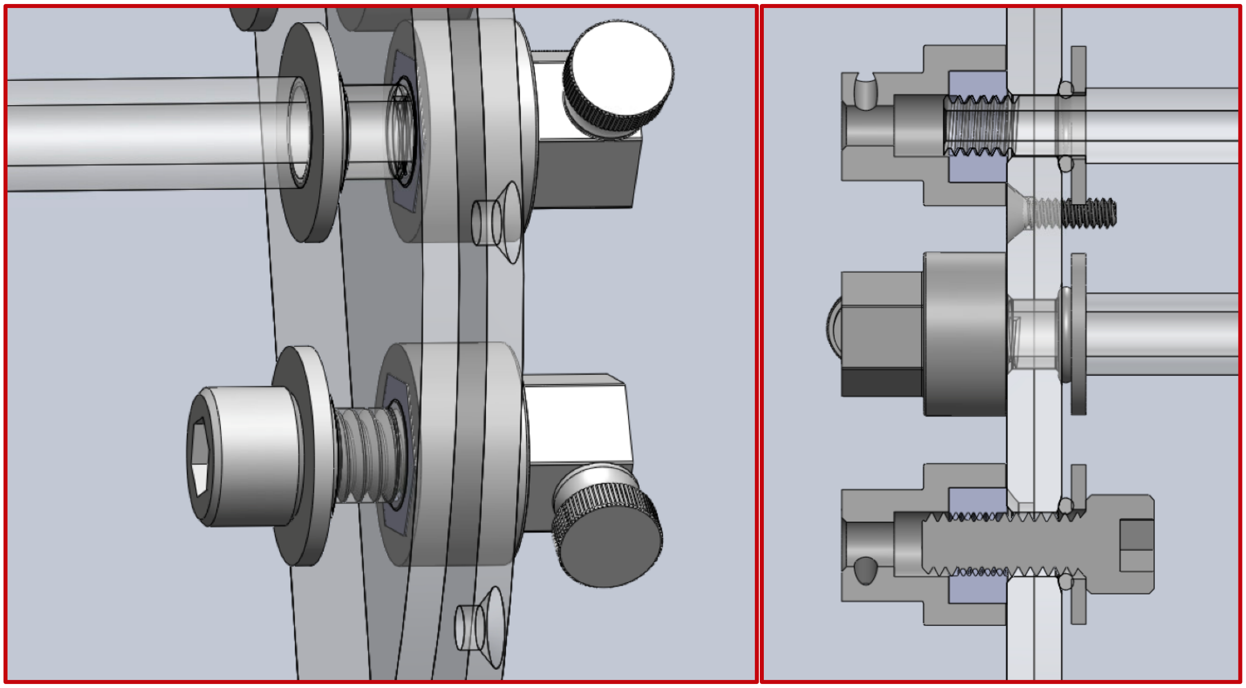

Figure 26. A 3D rendering of the assembled heart module (left) and section view (right) highlighting the interchangeable screw or cavity configurations for the novel phantom housing.

Radiation therapy involves precise targeting of tumors and sparing nearby organs at risk. This also requires precise treatment of targeted radiation. This phantom innovation is necessary for precise targeting and dose delivery to multiple points in simple or complex (e.g., anthropomorphic) geometries with one or multiple targets. Another opportunity is to use implanted anthropomorphic geometry that can flexibly demonstrate different human conditions to facilitate high-precision radiation therapy and mimic clinical use cases. The modular functionality also accommodates different radiation detectors or implants to allow for superior flexibility for imaging and measuring radiation doses and widen the applications over current market options. Extensions of this phantom may include but are not limited to, surgical planning, radiofrequency ablation procedures, metal artifact reduction imaging schemes, or interventional radiology applications.

The state-of-the-art flexible phantom module will be applied in the many settings as previously defined. In one permutation, it can be affixed to an existing ceramic motor to enable motion-resolved experimentation in many imaging modalities or radiation therapy. Tumor and normal organ surrogates can be implanted to mimic medical applications. The flexible phantom can be used to house measurement or targeting devices used for quality assurance procedures, to mimic a clinical workflow, or test new technological advances. Advanced medical applications can be designed such as implanting medical leads, implanting calcifications in an organ, or inserting metal implants such as those used in orthopedics. In imaging applications, tubing which incorporates moving or stationary fluids may be placed within the cavities for benchmarking techniques involving fluid flow.

7.3 Experimental Design for End-to-end Testing

7.3a Module Configurations

Once the designed modified hollow body oval and heart module are fabricated, a series of experiments will be conducted with the MR-compatible cardiac phantom. These experiments will integrate the many novel design characteristics of the heart phantom for cardiac applications in imaging and radiotherapy procedures. The phantom enables repeatable experimental conditions for both imaging and dosimetric testing on an anthropomorphic geometry affected by cardiac and respiratory motion. Due to manufacturing limitations, the first experimental implementation will contain a single access port with interchangeable dosimetry inserts for targeting regions of interest around the anthropomorphic geometry. The interchangeable inserts are projected to be capable of three configurations (Table 12).

For radiotherapy experiments, ion chamber measurements will be used for comparison to the HYPERSCINT^{TM} Research Platform 200 (HS-RP200, MedScint Inc., Quebec, Canada) scintillation detectors. Candidate chambers include the A1SLMR or A28MR (Standard Imaging, Wisconsin, USA) to reduce the number of changed variables in the experiment. Treatment plans will be generated using the same prescription dose parameters, but the resulting dose calculations and measurements are predicted to be slightly different due to the small geometric and material variations between detector size and type. Each experiment will be performed from start to finish without changing the dosimetry insert to reduce the variability of detector positioning in each configuration.

Projected Phantom Configurations and Reported Dosimeter Specifications for Future Dosimetry Experiments			
	Insert 1	**Insert 2**	**Insert 3**
Dosimeter	**A1SLMR (Ion Chamber)**	**A28MR (Ion Chamber)**	**HS-RP200 (Scintillator)**
Outer Diameter	6.35 mm	8.0 mm	5.0 mm
Collecting Volume	0.053 cc	0.125 cc	0.79 cc
Material	C552	C552	**Housing:** Proprietary plastic **Scintillator:** Proprietary polyvinyl toluene mix (near water equivalency)
Current Clinical Use	Daily QA	Monthly QA	Experimental only

Table 12. Three projected phantom configurations for dosimetry experiments. Each will be capable of consistent geometry except for small variability in the insert sizes due to the differences in the dosimeters' geometry. Therefore each will require separate imaging, treatment planning, and dose calculations by the TPS. Percent deviation from the planned dose while stationary or in motion will be evaluated in 5D motion-gated experiments.

7.3b Treatment Planning Workflows

The phantom may be imaged on a CT-SIM, 4DCT, 1.5T MR-simulator, or 0.35T MR-linac while either stationary or moving due to the multi-modality capabilities of the phantom components. This flexibility allows for many avenues of evaluation for clinical treatment plans. The first planned experiment using the anthropomorphic phantom will be performed using a patient-informed design. The treatment planning will use a recent ventricular tachycardia (VT) radioablation treatment delivered with respiratory gating on a TrueBeam Edge. First, images of the phantom will be acquired, then the experiment will be separated into two workflows. One will be an MR-only workflow while the other will include both MRI and CT as inputs for developing the treatment plan. Doses will be delivered and recorded using the plan developed from each workflow (Figure 27).

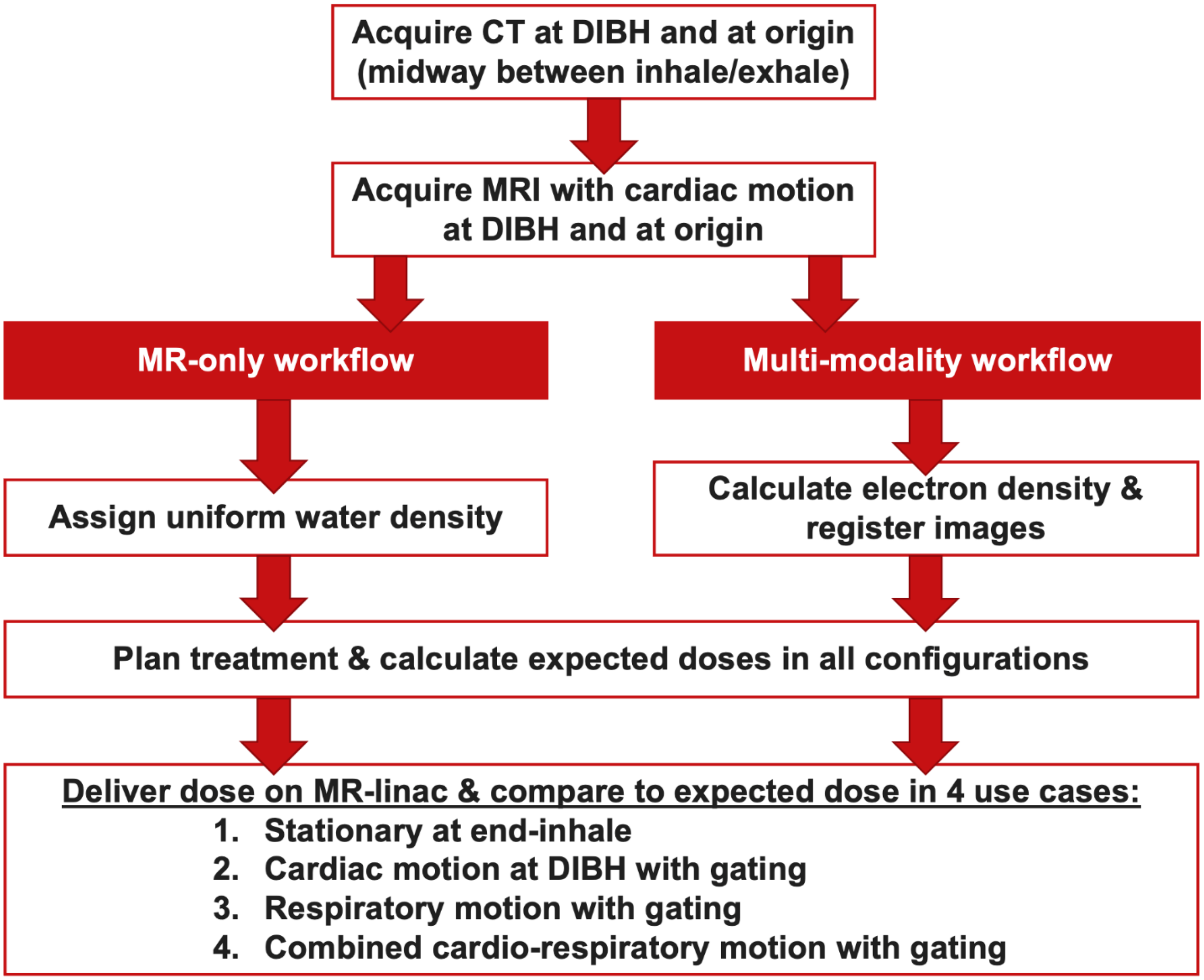

Figure 27. Workflow diagram describing the experimental design using the novel phantom module; treatments will be delivered using plans developed in MR-only and multi-modality clinical workflows. Respiration will follow a cos^4 waveform with 2 cm peak-to-peak motion and 15 breaths per minute. [23] Cardiac waveform will be approximated by data from Ouyang *et al*. [27]

First, the clinical standard thoracic CT imaging protocol at 120 kVp will be used for acquiring images with the module in the end-exhale position and origin positions. The origin in this case is defined as halfway between (1 cm away from) inhale and exhale positions. Then, images on the 0.35T MR-linac will be acquired using TrueFISP sequences in the same stationary positions and while moving with respiratory motion. The respiratory motion will follow a $\cos^4$ waveform with 2cm peak-to-peak motion and 15 breaths per minute which is often used to characterize respiratory motion. [23] Cardiac waveforms will be informed by experimental data from Ouyang *et al*. Alignment of crosshairs on the phantom's surface to external lasers in three dimensions will enable consistent placement of the phantom module within each imaging modality and for preparation in radiation delivery.

The treatment plans will be developed using the prescription dose and localization from a patient VT plan in an MR-only workflow as well as a multi-modality workflow using inputs from either of these scans. The MR-only workflow will assign a uniform electron density of water to the entire phantom. In the multi-modality workflow, the CT image will be used to calculate the electron density of the various phantom structures and registered to the phantom image in MR. Adjusting the electron density changes the calculated attenuation of the photon beam in the planning process, resulting in a different delivery plan to achieve the same prescription dose to the target volume than that which is planned in an MR-only workflow. Therefore, the treatment plan developed from the MR-only and multi-modality workflows will each need to be delivered and measured for comparison of dose between the two.

7.3c Plan Delivery and Dosimetric Evaluations

These treatment plans will be delivered in both stationary and moving configurations with a dosimeter placed in the dose gradient region or near the edge of the target volume to effectively compare planned and delivered doses. The calculated value in the treatment planning system (TPS) at the location of the dosimeter will be compared to the dose from the gated delivery. To study the differences in planned and delivered doses in each configuration and workflow, the percent deviation as a ratio of the delivered dose to the planned dose will be calculated. The expectation is the delivered dose in the DIBH configuration and during respiratory motion with gating should match closely (i.e., low percent deviation) to the calculated dose from the TPS.

The hypothesis is that deliveries with improper gating instances can be detected with the real-time scintillation detectors and may result in an increase in delivered dose outside the target volume, with a reduction of dose inside the target volume. Plans which have a higher number of improper gated deliveries are expected to have a higher percent difference. Additionally, the complex motion which includes both cardiac and respiratory-induced excursions may reduce delivery efficiency and result in a higher number of improper gated deliveries.

The results from the outlined experiment will provide more insight into the impact of cardiac or respiratory-induced excursions on calculated doses in a gated ventricular tachycardia radioablation treatment. It will also be able to show differences in planned and delivered doses between MR-only or multi-modality workflows in radiotherapy. The first-time use of this motion-capable anthropomorphic phantom integrated with real-time scintillation dosimeters and ion chambers will provide useful evaluation metrics for plan efficiency and dose delivery of a high-precision radiotherapy procedure.

7.4 Preliminary Dosimetric Validation of Scintillators in a 0.35T MR-linac

7.4a Dosimetry in a Magnetic Field

MR-guided radiotherapy (MRgRT) enables real-time gating and online adaptation leading to improvement of treatment outcomes due to more accurate targeting of tumors and avoidance of critical structures in the delineation of soft tissues. To evaluate the doses delivered in MRgRT, unique dosimeters are required due to the high magnetic fields required for imaging. Not only must the MR compatibility of the detectors be considered in this environment, but magnetic fields have also been observed to increase the dose at air-tissue interfaces due to the electron return effect. This is attributed to the well-known Lorentz force ($\vec{F}_B$) acting on secondary electrons with elementary charge (e^-) produced in the radiation field, defined in equation (10)

$$\vec{F}_B = e^-\left(E + \vec{v} \times \vec{B}_{ext}\right) \tag{10}$$

When a charged particle moves in the presence of an external magnetic field ($\vec{B}_{ext}$), a force is exerted perpendicular to the velocity ($\vec{v}$) which causes the trajectory of this particle to move in a helical path. In homogeneous media, this effect is negligible but increases in severity at tissue-air interfaces due to the increased mean free path of electrons in air allowing for the helical path of the electrons to return to the proximal side of the interface. [73] This effect generally causes the dose in the thoracic region to be elevated at the superficial regions of the lung and reduced at the deep interfaces.

Another undesired outcome of the electron return effect is the directional dependence of measurements obtained with MR-compatible ion chambers within a magnetic field. [74] This is primarily due to the helical trajectory of the electrons or positrons used for charge collection in the air-filled chamber volume. Since the force acting upon these particles is perpendicular to the external magnetic field, changes in orientation with respect to the field will cause changes in the measured inductance caused by the charged particles used for the calculation of dose.

To overcome some of the challenges of working in a magnetic field, scintillation detectors made of near water-equivalent materials are presented as an alternative to ion chambers. Scintillators are a class of materials that rapidly emit optical photons in response to high-energy radiation. As such, they do not require a bias voltage which can affect MR image quality, nor do they rely on an air cavity for charge collection. These detectors are MR-safe, water-equivalent, and have been shown to have little directional dependence within a magnetic field. [75]

The near-water equivalence of the detector probes minimizes electron return effects and beam disturbance. The specific materials used for the scintillator are comprised of a proprietary polyvinyltoluene mix that is surrounded by a proprietary plastic mix to form the probe end. The sensitive volume of the probe end is optically coupled to a long fiberoptic cable between 20 and 30 meters in length which feed to the readout device and utilizes the hyperspectral approach. [76]

7.4b Experimental Methods

To demonstrate the viability of future use in the designed phantom, the first implementation of the HYPERSCINT^{TM} Research Platform 200 (HS-RP200, MedScint Inc., Québec, Canada) scintillation dosimeters were conducted on a commercially available motion insert for gating experiments in a low-field MR-linac. First, each scintillator detector underwent standard spectral calibrations using a Varian TrueBeamSTX and dose calibrations on a ViewRay MR-Linac. [77]

Following manufacturer recommendations, the spectral calibrations involved 3 configurations named scintillation, fluorescence, and Cerenkov, performed on a Varian TrueBeamSTX. The scintillation (probe end) and fluorescence (optical fiber) calibrations used the linac-integrated kV imager in continuous mode, with the highest possible output and no filter, irradiating the probe end and optical fibers in the two configurations respectively, and collecting calibration data (v1.2; MedScint Inc., Québec, Canada). The Cerenkov calibrations were performed for the optical fibers by placing the fibers horizontally in the center of a 10x10cm field size along the top of a 20x20cm solid water dosimetry block with 2cm thickness, while placing the probe tips at 0.5m and 1.5m away from the center of the field. The linac gantry was positioned at 45° and 315° for 4 total irradiations by a 6 MV beam at dose rate 600 MU/min.

The dose calibration was performed for each of 4 probe tips individually on a 0.35T MR-linac directly before the experiments took place. The probe end was placed in the center of a

30x30cm solid water block via a tight-fitting bore, placed at the central axis of the MR-linac. A stack of solid water blocks were placed on top of this for the probe to be at 10cm depth. The readout system was activated for a dose calibration measurement and irradiated with 500 MU at 600MU/min in a 10x10cm field size. The reading from the scintillation detector was calibrated to the dose expected in this configuration.

Four scintillator detectors were taped in or around the motion phantom for simultaneous readout during the experiment. Channel 3 was centered in the moving cuboid insert at its deepest point (Figure 28, A), while Channels 1, 2, and 4 were stationary on the top external surface of the hollow body oval (Figure 28, B and C). The center of the phantom was placed in beam isocenter with the motor output having a $\cos^4$ waveform and 3 cm peak-to-peak amplitude at 12 breaths per minute to simulate respiratory motion. [23]

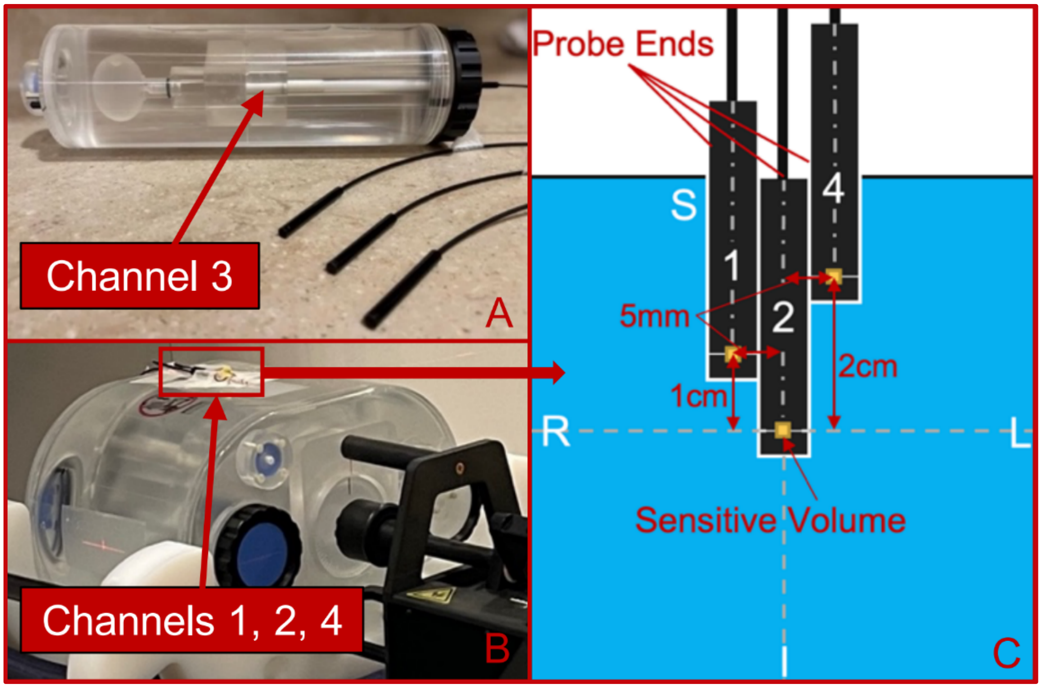

Figure 28. MR-compatible insert used for 4 multi-point scintillator detectors used in gating experiments. Channel 3 is attached to an MR-safe programmable motor (A). Channels 1, 2, and 4 are stationary on the phantom surface (B) in the configuration shown in C, where channel 2 is at the center of the phantom.

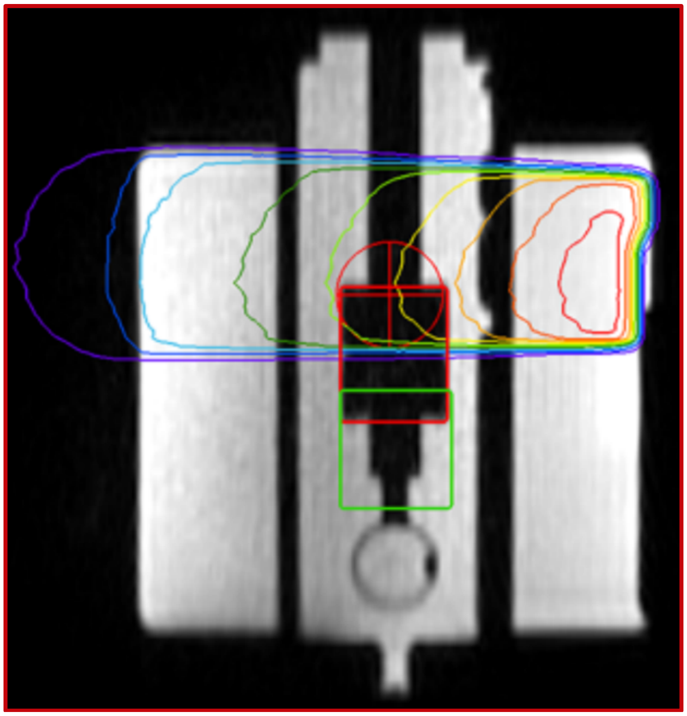

Figure 29. Coronal view of the motion gating phantom with treatment plan overlay and marked isocenter indicating the high dose gradient for channel 3.

Two gated treatment plans were generated at 4 Gy per fraction with Channel 3 placed in the center of the target or the gradient region (penumbra) to enable two sets of experiments (Figure 29). To create a gated treatment plan, the motion-capable cuboid that contained the dosimeter was defined as the region of interest. Gating parameters for motion tracking systems can be defined by two numbers: (1) a gating margin in mm that is an expansion of original structure contours, and (2) a percent overlap describing the threshold acceptable area of the region of interest which has left the collimated beam area. Based upon recent literature articles that use a 0.35T MR-linac for SBRT, a typical gating margin of 3mm and 5 or 10% overlap seems to be the current standard-of-care protocol for high-precision gated treatments. [78, 79] Considering these ranges, four gating parameters for the gated delivery were chosen: expansion margins of 3 or 5 mm and 5% or 10% overlaps. These parameters were used to evaluate gating performance and tracking efficacy via the time-resolved detectors.

7.4c Results, Discussion, and Future Work

The table below highlights the summarized readouts for each of the gating experiments and parameters, suggesting reliable readings even in the presence of motion in the gradient region. The results from this table show the capability of the scintillation dosimeters to detect gating instances in the configurations where the dosimeter is moving in the central and gradient regions of the treatment plan. The number of gating instances and total duration of delivery for an otherwise equivalent plan describe the gating efficiency of the delivery. Many gating instances and high duration implies worse efficiency.

	CENTRAL AXIS			GRADIENT (PENUMBRA)		
Gating Parameter	**Number of Gating Instances**	**Total Duration (s)**	**Channel 3 Cumulative Dose (cGy)**	**Number of Gating Instances**	**Total Duration (s)**	**Channel 3 Cumulative Dose (cGy)**
10%-5mm	**22**	**108.2**	**386.0**	**22**	**107.2**	**122.1**
10%-3mm	**24**	**117**	**385.8**	**24**	**117.9**	**124.5**
5%-5mm	**27**	**129.9**	**385.6**	**27**	**130.4**	**123.3**
5%-3mm	**26**	**128**	**385.3**	**27**	**132.4**	**124.3**

Table 13. Results for gating experiments using a scintillation detector placed at the central axis and in the dose gradient (penumbra).

Placement of the scintillator at the central axis and gradient region yielded results indicating efficient radiation deliveries for the largest overlap and margin parameters of 10%-5mm with 22 gating instances in 108 seconds. Using the more restrictive overlapping parameter of 5%, efficiency was decreased between 26-27 gating instances in approximately 130 seconds for the 5mm and 3mm margins. The 10%-3mm gating parameter resulted in an intermediate efficiency with 24 gating instances in approximately 118 seconds.

All gating experiments resulted in an equivalent cumulative dose for central axis measures.

In the central axis, cumulative dose varied by less than 0.7 cGy (0.2%). In the gradient sampled area, the dose deviated by less than 4 cGy (2%). These results suggest stable dosimeter readings and effective gating procedures useful for validation of these dosimeters in this configuration and viability for the designed phantom.

Figure 30 shows the high temporal resolution detection at multiple positions for the central and gradient regions. Note the reduced dose when the detector was in the gradient region and the ability of the multi-point detectors to detect a spurious beam-on incident when the tracking algorithm failed (Figure 30, right) suggesting strong potential for use of the real-time readout for quality assurance of gating and tumor tracking in MR-linacs. Four spurious beam-on incidents were detected with real-time readout at 10%-3mm and 5%-5mm margins.

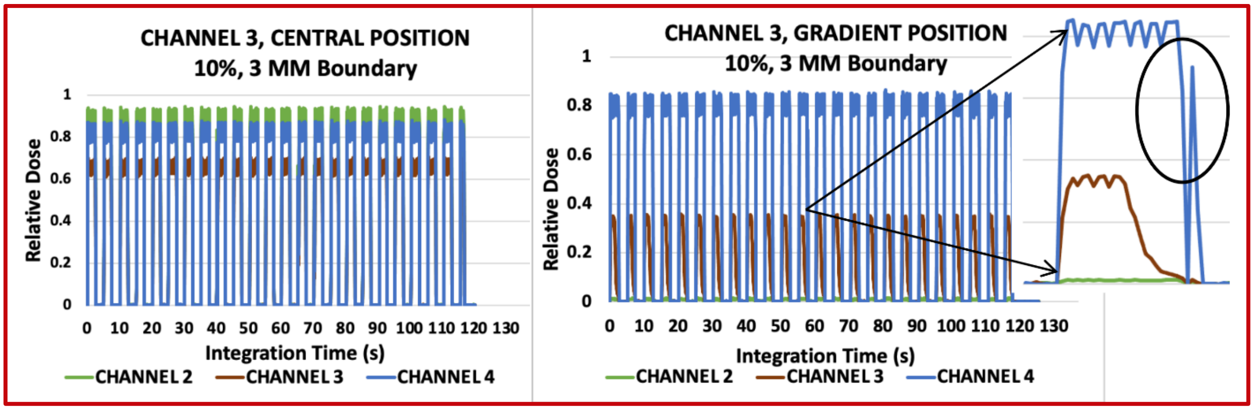

Figure 30. (Left) Three-channel readout with red channel 3 at the (left) central, (middle) gradient position, and zoomed-in figure (right) of a triggering event that occurred due to an improper tracking frame on a cine MRI dataset, underscoring the potential of using multi-point detectors to detect erroneous results and confirm tracking algorithm and gating capabilities of MR-linacs.

The time-resolved and multi-point dosimetry system shows considerable promise for use in low-field MR-Linac settings. No image artifacts from the scintillation system were apparent in the MR-linac image acquisitions in any sequence. The lack of artifacts indicates these detectors will be useful for dosimetry during online imaging of more complex and moving geometries such as for the heart module. While cumulative dose was not impacted by tighter margin conditions in this apparatus during motion prescription, gating efficiency was negatively impacted. Identifying spurious beam-on incidents via this methodology offers the potential for gating commissioning and tracking algorithm verification. Improper gating incidents may be flagged by a stationary detector on the surface, supplemented by a lack of dose detected in the moving insert, and confirmed by a review of recorded gating videos.

As a preliminary evaluation, this study did not include repeated measurements under the same conditions. Although more rigorous scientific experiments would include multiple trials to evaluate repeatability, the purpose of the preliminary evaluations using these dosimeters is for proof-of-concept verification in the proposed use of these detectors for the final phantom module. The experiment has verified that the novel multi-point scintillation detectors can yield useful results from motion gating experiments on an MR-linac.

Future work involves the integration of these detectors in the anthropomorphic heart module with more complex geometries and motions. Validation of the real-time dosimeters will occur via the end-to-end experimental design which will be completed after the submission of this thesis.

8 | Conclusions and Future Work

8.1 Limitations and Future Work

8.1a Heart Model Improvements

The 3D heart model and contours were derived from a contrast-enhanced CTCA scan, acquired and reconstructed during the 90% frame. This frame was originally chosen because it correlates to end-ventricular diastole (filling). At the beginning of the project, the projected design configuration incorporated compressive deformable motion. When considering that the heart will deform into a compressed state, images were chosen to simulate the maximum filling of the LV in its relaxed state, so that compression would simulate the natural contraction of the LV. However, considerations were not made about atrial systole (contraction).

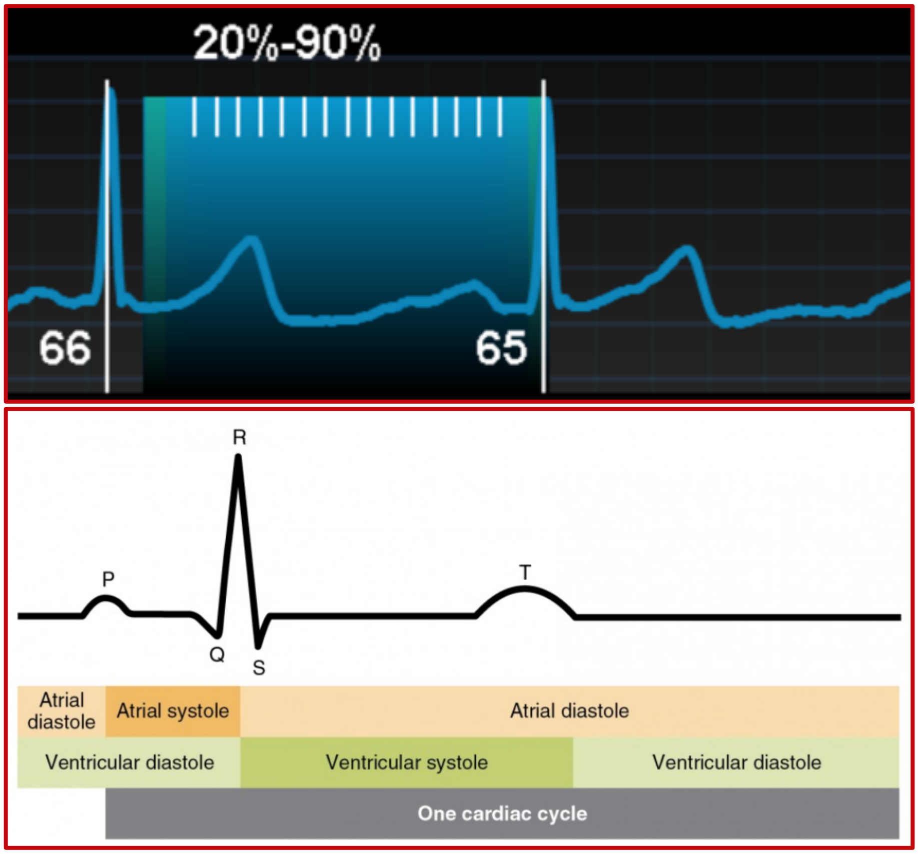

Figure 31. Electrocardiography (ECG) waveform acquired during the contrast-enhanced CTCA used for the heart model (top) and phases of heart motion corresponding to the ECG signal. [80]

Future implementations may incorporate additional feedback from the cardiovascular radiologist to evaluate different percent phase that correlates to end-diastole (65-75%) for both the atria and the ventricles. Nevertheless, cardiac motion occurs in the 90% frame due to the beginning of atrial systole, which causes movement of the coronary arteries (Figure 31). [80] This causes difficulty in contouring and may introduce motion artifacts and noise to the image. In some cases, the coronary arteries may appear disjunct from slice to slice because of this motion. Overall, the model may be improved by using a different percent phase for the scan. Alternative strategies include utilizing a computational phantom with moving cardiac substructures as in Morton *et al* for a matching 3D-printed model. [31] This would allow for validation of 5DCT acquired in virtual simulations by matching these data to the physical acquisitions with the printed model.

8.1b Module Motion and ECG Simulation

To mimic a moving heart with the rotational degrees of freedom afforded by the MR-safe motor, approximate motion parameters were derived from literature. [23, 27] While the waveforms used for motion prescription are accurate according to the literature, some limitations exist in using these to prescribe movements to the heart module. Superoinferior centroid movement of the LV at DIBH reported by Ouyang *et al* likely underestimates the excursions of the whole heart. To rectify this underestimation of heart motion, considerations are made to scale the amplitude of this waveform to resemble patient-specific excursions using a novel 5D MRI sequence currently used in research.

This technology is also considered for matching the excursions of the heart to a simulated output ECG waveform. The output ECG waveform would give additional flexibility for the phantom to be imaged in the 5D MRI or 4DCT applications that gate based upon the electrical signals of the heart. Additionally, this phantom could be used to evaluate the potential capabilities of delivering radiation with ECG-gating given this simulated ECG waveform.

8.1c Localization of Dosimeters

In radiation dosimetry, precise localization of the point of measurement is critical for comparing the predicted dose against values obtained from a dosimeter. Therefore, the phantom housing that is being fabricated now would benefit from a measurement instrument with an atlas to map the depth of the dosimeter within the cavity to the surrounding model geometry. If a planned experiment is to simulate radiation treatment, dosimeters ought to be placed precisely around the target area in a dose fall-off region to produce meaningful results.

There are several proposed methods for the localization of the dosimeters within the phantom. The localization methods must be MR-compatible and maintain the flexibility of the module for many use cases. The first few ideas for indexing the phantom involve cylindrical plastic spacers or a singular rod with ruled markings or grooves with known spacing to help with positioning within the phantom. Each of these options would be capable of being held in place by the set screws at the end caps of the phantom. These indexers may be made of acrylic or otherwise water-equivalent material to minimize beam disturbance by the cavities. Some of the indexers may also be machined to sit flush around the rounded tip geometry of an ion chamber to further reduce beam disturbance and electron return effect.

8.2 Conclusions

The experiment outlined in the prior chapter will prove the efficacy of the fabricated cardiac phantom for dosimetric evaluations of a respiratory-gated ventricular tachycardia (VT) treatment plan that was given to a patient. The comparison between MR-only and multi-modality treatment workflows made possible by the unique phantom is just one example of an experiment made possible by this phantom. While the first experiment with the novel cardiac phantom is for radiotherapy applications, the phantom module with complex motion may also be used for benchmarking 5D MRI sequences, 4DCT imaging, 4D-CBCT, or experiments involving other anthropomorphic geometries.

The simulated phantom design is projected to fulfill each of the eight design goals set at the beginning of the project with ample flexibility for many uses and potential for improvements. The material selected for model fabrication is accessible and capable of producing a complex anthropomorphic geometry that is visible in CT, 1.5T MRI, or 0.35T MRI against a water background. The modular phantom housing allows for implementation for many use cases including imaging and radiotherapy, while being retrofitted to a MR-compatible motor to enable experiments involving motion. Dosimetry during motion at multiple locations throughout a similar phantom was performed to verify the capabilities of the current equipment to be used for image-guided radiation therapy experiments after integration with the prototype phantom fabrication.

Overall, the designed phantom will provide excellent flexibility and utility when compared to current market options to aid experiments in radiotherapy and imaging. The interchangeable anthropomorphic geometry allows for the design to be utilized for a variety of body sites. High-precision applications of modern radiotherapy and imaging will benefit from the advancements made in the completion of this thesis.

References

1. Siegel RL, Miller KD, Wagle NS, Jemal A. Cancer Statistics, 2023. *CA Cancer J Clin.* 2023;73(1):17-48.

2. Raghunathan D, Khilji MI, Hassan SA, Yusuf SW. Radiation-induced cardiovascular disease. *Current Atherosclerosis Reports*. 2017;19(22).

3. Brown KN, Hussain K, Richards JR. Radiation Induced Coronary Artery Disease. *StatPearls*. Treasure Island (FL): StatPearls Publishing; 2022.

4. Filopei J, Frishman W. Radiation-induced heart disease. *Cardiology in Review*. July/August 2012;20(4):184-188.

5. Om A, Ellahham S, Vetrovec GW. Radiation-induced coronary artery disease. *American Heart Journal*. December 1992;124(6):1598-1602.

6. Anderson R, Wethal T, Günther A, et al. Relation of coronary artery calcium score to premature coronary artery disease in survivors >15 years of Hodgkin's lymphoma. *American Journal of Cardiology*. 15 2010;105(2):149-152.

7. van Nimewegan FA, Schaapveld M, Cutter DJ, et al. Radiation Dose-Response Relationship for Risk of Coronary Heart Disease in Survivors of Hodgkin Lymphoma. *Journal of Clinical Oncology*. January 2016;34(3):235-243.

8. Morton DL, Glancy DL, Joseph WL, Adkins PC. Management of patients with radiation-induced pericarditis with effusion: a note on the development of aortic regurgitation in two of them. *Chest*. September 1973;64(3):291-297.

9. Zindler JD, Thomas CRJ, Hahn SM, Hoffmann AL, Troost EG, Lambin P. Increasing the therapeutic ratio of stereotactic ablative radiotherapy by individualized isotoxic dose prescription. *Journal of the National Cancer Institute*. October 2015;108(2):djv305.

10. Gagliardi G, Constine LS, Moiseenko V, et al. Radiation dose-volume Effects in the heart. *International Journal of Radiation Oncology, Biology, Physics*. 2010;76(3):S77-S85.

11. Banfill K, Giuliani M, Aznar M, et al. Cardiac toxicity of thoracic radiotherapy: existing evidence and future directions. *Journal of Thoracic Oncology*. November 2020;16(2):216-227.

12. Bradley JD, Hu C, Komaki RR, et al. Long-term results of NRG Oncology RTOG 0617: Standard- versus high-dose chemoradiotherapy with or without cetuximab for unresectable stage III non-small-cell lung cancer. *Journal of Clinical Oncology*. December 2019;38(7):706-715.

13. McWilliam A, Abravan A, Banfill K, Faivre-Finn C, van Herk M. Demystifying the results of RTOG 0617: Identification of dose sensitive cardiac subregions associated with overall survival. *Journal of Throacic Oncology*. May 2023;18(5):539-664.

14. Bergom C, Bradley JA, Ng AK, et al. Past, present, and future of radiation-induced cardiotoxicity: refinements in targeting, surveillance, and risk stratification. *Journal of the American College of Cardiology: CarioOncology*. September 2021;3(3):343-359.

15. Harms J, Zhang J, Kayode O, et al. Implementation of a knowledge-based treatment planning model for cardiac-sparing lung radiation therapy. *Advances in Radiation Oncology*. 2021;6:100745.

16. Morris ED, Aldridge K, Ghanem AI, Zhu S, Glide-Hurst CK. Incorporating sensitive cardiac substructure sparing into radiation therapy planning. *Journal of Applied Clinical Medical Physics*. 2020;21(11):195-204.

17. Cuculich PS, Schill MR, Kashani R, et al. Noninvasive Cardiac Radiation for Ablation of Ventricular Tachycardia. *The New England Journal of Medicine*. December 2017;377(24):2325-2336.

18. Varian Medical Systems, Inc. About Varian: Newsroom Press Releases. *Varian: A Siemens Helthineers Company*. January 19, 2023. Available at: **https://www.varian.com/about-varian/newsroom/press-releases/varian-receives-investigational-device-exemption-cardiac**. Accessed April 2023.

19. Modus QA Product Data Sheet MRI4D Inserts. *Modus QA*. 2020. **https://modusqa.com/wp-content/uploads/2020/09/Modus-QA-Product-Data-Sheet-MRI4D-Inserts.pdf**. Accessed July 2022.

20. Mutic S, Palta JR, Bukter EK, et al. *Quality assurance for computed-tomography simulators and the computed-tomography-simulation process*: American Association of Physicists in Medicine; 2003. Task Group No. 66.

21. Mayo CS, Moran JM, Bosch W, et al. *Standardizing nomenclatures in radiation oncology*: American Association of Physicists in Medicine; 2018. Task Group No. 263.

22. Spodick DH, Raju P, Bishop RL, Rifkin RD. Operational definition of normal sinus heart rate. *The American Journal of Cardiology*. May 1992;69(14):1245-1246.

23. Lujan AE, Larsen EW, Balter JM, Ten Haken RK. A method for incorporating organ motion due to breathing into 3D dose calculations. *Medical Physics*. May 1999;26(5):715-720.

24. Lujan AE, Balter JM, Ten Haken RK. A method for incorporating organ motion due to breathing into 3D dose calculations in the liver: sensitivity to variations in motion. *Medical Physics*. October 2003;30(10):2643-49.

25. Keall PJ, Mageras GS, Balter JM, et al. *The management of respiratory motion in radiation oncology*. College Park, MD: American Association of Physicists in Medicine; 2006. Task Group Report no 91.

26. Henke LE, Contreras JA, Mazur T, et al. Delineation of a cardiac planning organ-at-risk volume using real-time magnetic resonance imaging for cardiac protection in thoracic and breast radiation therapy. *Practical Radiation Oncology*. 2019;9:e298-e306.

27. Ouyang Z, Schoenhagen P, Wazni O, et al. Analysis of Cardiac Motion without Respiratory Motion for Cardiac Stereotactic Body Radiation Therapy. *Journal of Applied Clinical Medical Physics*. July 2020;21(10):48-55.

28. Rit S, van Herk M, Zijp L, Sonke JJ. Quantification of the variability of diaphragm motion and implications for treatment margin construction. *International Journal of Radiation Oncology, Biology, Physics*. 2012;82(3):e399-e407.

29. Lorenz CH, Pastorek JS, Bundy JM. Delineation of normal human left ventricular twist throughout systole by tagged cine magnetic resonance imaging. *Journal of Cardiovascular Magnetic Resonance*. 2000;2(2):97-108.

30. Srinivasan K, Mohammadi M, Shepherd J. Applications of linac-mounted kilovoltage Cone-beam Computed Tomography in modern radiation therapy: A review. *Polish Journal of Radiology*. July 2014;79(181-193):181-193.

31. Morton N, Keall P, O'Brien R, Reynolds T. CArdiac and REspiratory adaptive Computed Tomography (CARE-CT): a proof-of-concept digital phantom study. *Physical and Engineering Sciences in Medicine*. 2022;45(1257).

32. Shrestha S, Gupta AC, Bates JE, et al. Development and validation of an age-scaleable cardiac model with substructures for dosimetry in late-effects studies of childhood cancer survivors. *Radiotherapy and Oncology*. October 2020;153:163-171.

33. Kortelainen MJ, Koivumäki TM, Vauhkonen MJ, Hakulinen MA. Effect of respiratory motion on cardiac defect contrast in myocardial perfusion SPECT: a physical phantom study. *Annals of Nuclear Medicine*. 2019;33:305-316.

34. Tavakoli MB, Taheri H, Akhavan A. Measurement of ipsilateral lung and heart dose in radiotherapy of left sided mastectomy patients in common different clinical techniques: a phantom study. *International Journall of Radiation Research*. July 2018;16(3):389-394.

35. Bolwin K, Czekalla B, Frohwein LJ, Büther F, Schäfers KP. Anthropomorphic thorax phantom for cardio-respiratory motion simulation in tomographic imaging. *Physics in Medicine and Biology*. January 2018;63:12pp.

36. Huang C, Petibon Y, Ouyang J, et al. Accelerated acquisition of tagged MRI for cardiac motion correction in simultaneous PET-MR: phantom and patient studies. *Medical Physics*. 2015;42:1087-97.

37. De Deene Y, Hill R, Skyt PS, Booth J. Flexydos3D: a new deformable anthropomorphic 3D dosimeter readout with optical CT scanning. Paper presented at: Journal of Physics: 8th International Conference on 3D Radiation Dosimetry (IC3DDose), 2014; Ystad, Sweden.

38. Swailes NE, MacDonald ME, Frayne R. Dynamic phantom with heart, lung, and blood motion for initial validation of MRI techniques. *Journal of Magnetic Resonance Imaging*. 2011;34:941-946.

39. Kee S, Larsen E, Paluch K, et al. Development of a dynamic heart phantom prototype for magnetic resonance imaging. Paper presented at: IEEE 36th Annual Northeast Bioengineering Conference, 2010; New York, NY.

40. Groen JM, van der Vleuten PA, Greuter MJ, Zijlstra F, Oudkerk M. Comparison of MRI, 64-slice MDCT, and DSCT in assessing funcitonal cardiac parameters of a moving heart phantom. *European Radiology*. 2009;19:577-583.

41. Boutchko R, Balakrishnan K, Gullberg GT, O'Neil JP, Inventors. Human torso phantom for imaging of heart with realistic modes of cardiac and respiratory motion. US8535061B2. September 17, 2013.

42. Huyer LD, Montgomery M, Zhao Y, et al. Biomaterial based cardiac tissue engineering and its applications. *Biomed Mater*. 2015;10(3):034004.

43. Barbosa JG, Figueiredo B, Bettencourt N, Tavares JM. Towards automatic quantification of the epicardial fat in non contrasted CT images. *Comput Methods Biomech Biomed Engin.* 2011;14(10):905-914.

44. McGarry CK, Grattan LJ, Ivory AM, et al. Tissue Mimicking Materials for Imaging and Therapy Phantoms; A Review. *Phys. Med. Biol.* 2020;65(23):TR01.

45. Isoda H. Sequential MRI and CT monitoring in cryosurgery—An experimental study in polyvinyl alcohol gel phantom. *PubMed*. 1989;49(9):1096-1101.

46. Thermoplastic Elastomer, Melt-Processible Rubber. *MatWeb: Material Property Database*. Accessed July 2022.

47. Song SJ, Choi J, Park YD, et al. Sodium alginate hydrogel-based bioprinting using a novel multinozzle bioprinting system. *Artificial Organs*. 2011;35(11):1132-1136.

48. Yeung RA, Kennedy RA. A comparison of selected physico-chemical properties of calcium alginate fibers produced using two different types of sodium alginate. *Journal of the Mechanical Behavior of Biomedical Materials*. February 2019;90:155-164.

49. Hartley C, Ng KL, Jackson A. CT and MR Appearance of Otolaryngologic Packing Materials. *American Journal of Neuroradiology*. September 1995;16:1697-1702.

50. Lam K. MO-F-CAMPUS-I-03: CT and MR Characteristics of Some Specialty 3D Printing Filaments. *Medical Physics*. June 2015;42(6):3579.

51. Neumann W, Pusch TP, Siegfarth M, Schad LR, Stallkamp JL. CT and MRI compatibility of flexible 3D-printed materials for soft actuators and robots used in image-guided interventions. *Medical Physics*. December 2019;46(12):5488-5498.

52. Dodge TJ, Brown GB, Bolson EL, Dodge HT. Lumen diameter of normal human coronary arteries: influence of age, sex, anatomic variation, and left ventricular hypertrophy or dilation. *Circulation*. July 1992;86(1):232-246.

53. Shinohara RT, Sweeney EM, Goldsmith J, et al. Statistical normalization techniques for magnetic resonance imaging. *Neuroimage: Clinical*. 2014;6:9-19.

54. Ammari S, Pitre-Champagnat S, Dercle L, et al. Influence of magnetic field strength on magnetic resonance imaging raiomics features in brain imaging, an in vitro and in vivo study. *Frontiers in Oncology*. January 2021;10:541663.

55. Wahid KA, He R, McDonald BA, et al. Intensity standardization methods in magnetic resonance imaging of head and neck cancer. *Physics and Imaging in Radiation Oncology*. 2021;20:88-93.

56. Gach HM, Curcuru AN, Wittland EJ, et al. MRI quality control for low-field MR-IGRT systems: lessons learned. *Journal of Applied Medical Physics*. September 2019;20(10):53-66.

57. Lewis BC, Shin J, Maraghechi B, et al. Assessment of a novel commercial large field of view phantom for comprehensive MR imaging quality assurance of a 0.35T MRgRT system. *Journal of Applied Clinical Medical Physics*. April 2022;23(4):e13535.

58. Centers for Disease Control and Prevention. About Adult BMI. *CDC Government Web site*. June 3, 2022. Available at: **https://www.cdc.gov/healthyweight/assessing/bmi/adult_bmi/index.html**. Accessed April 2023.

59. Feng M, Moran JM, Koelling T, et al. Development and validation of a heart atlas to study cardiac exposure to radiation following treatment for breast cancer. *Int. J. Radiation Oncology Biol. Phys.* 2011;79(1):10-18.

60. Serra J. Introduction to mathematical morphology. *Computer Vision, Graphics, and Image Processing*. 1986;35:283-305.

61. Milo MLH, Nyeng TB, Lorenzen EL, Hoffmann L, Møller DS, Offersen BV. Atlas-based auto-segmentation for delineating the heart and cardiac substructures in breast cancer radiation therapy. *Acta Oncologica*. 2022;61(2):247-254.

62. Taubin G. Curve and surface smoothing without shrinkage. *Institute of Electrical and Electronics Engineers*. 1995:852-857.

63. Csige I, Ujvárosy , Szabó Z, et al. The Impact of Obesity on the Cardiovascular System. *Journal of Diabetes Research*. 2018;2018:1-12.

64. Fuchs A, Mejdahl MR, Kühl JT, et al. Normal values of left ventricular mass and cardiac chamber volumes assessed by 320-detector computed tomography angiography in the Copenhagen General Population Study. *European Heart Journal - Cardiovascular Imaging*. September 2016;17(9):1009-1017.

65. Socha J, Rygielska A, Uzięcbło-Życzkowska B, et al. Contouring cardiac substructures on average intensity projection 4D-CT for lung cancer radiotherapy: A proposal of a heart valve contouring atlas. *Radiotherapy and Oncology*. February 2022;167:261-268.

66. Finnegan RN, Chin V, Chlap P, et al. Open-source, fully-automated hypbrid cardiac substructure segmentation: development and optimisation. *Physical and Engineering Sciences in Medicine*. 2023;46:377-393.

67. Garcia J, Yang Z, Mongrain R, Leask RL, Lachapelle K. 3D printing materials and their use in medical education: a review of current technology and trends for the future. *BMJ Simulation & Technology Enhanced Learning*. 2018;4(1):27-40.

68. FormLabs, Inc. Material Data Sheet: Elastic 50A

69. Li S, Yuan S, Zhu J, Wang C, Li J, Zhang W. Additive manufacturing-driven design optimization: Building direction and structural topology. *Additive Manufacturing*. December 2020;36.

70. Ahn SH, Montero M, Odell D, Roundy S, Wright PK. Anisotropic material properties of fused deposition modeling ABS. *Rapid Prototyping Journal*. 2002;8(4):248-257.

71. Tian J, Li M, Han Z, et al. Conformal topology optimization of multi-material ferromagnetic soft active structures using an extended level set method. *Computer Methods in Applied Mechanics and Engineering*. August 2022:Preprint.

72. Lee HH. *Finite Element Simulations with ANSYS Workbench 2019: Theory, applications, case studies.* Mission: SDC Publications; 2019.

73. Raaijmakers AJE, Raaymakers BW, Lagendijk JJW. Integrating a MRI scanner with a 6 MV radiotherapy acceleratory: dose increase at tissue-air interfaces in a lateral magnetic field due to returning electrons. *Physics in Medicine and Biology*. 2005;50:1363-1376.

74. Shulka BK, Spindeldreier CK, Schrenk O, et al. Dosimetry in magnetic fields with dedicated MR-compatible ionization chambers. *Physica Medica*. 2020;80:259-266.

75. Uijtewaal P, Côté B, Foppen T, et al. Performance of the HYPERSCINT scintillation dosimetry research platform for the 1.5 T MR-linac. *Physics in Medicine and Biology*. February 2023;68:04NT01.

76. Therriault-Proulx F, Archambault L, Beaulieu L, Beddar S. Development of a novel multi-point plastic scintillation detector with a single optical transmission line for radiation dose measurement. *Physics in Medicine and Biology*. 2012;57:7147-7159.

77. MEDSCINT Inc. HYPERSCINT(TM) Research Platform 200 Instructions for Use. 01st ed. Québec QC, Canada; 2022.

78. Ehrbar S, Käser SB, Chamberlain M, et al. MR-guided beam gating: Residual motion, gating efficiency and dose reconstruction for stereotactic treatments of the liver and lung. *Radiotherapy and Oncology*. September 2022;174:101-108.

79. Palacios MA, Verheijen S, Schneiders FL, et al. Same-day consultation, simulation and lung Stereotactic Ablative Radiotherapy delivery on a Magnetic Resonance-linac. *Physics and Imaging in Radiation Oncology*. October 2022;24:76-81.

80. Lumen Learning. Anatomy and Physiology II Module 3: The Cardiovascular System: The Heart. *Lumen Learning Courses*. 2023. Available at: **https://courses.lumenlearning.com/suny-ap2/chapter/cardiac-cycle/**. Accessed April 2023.